Research Square

Preprints are preliminary reports that have not undergone peer review.
They should not be considered conclusive, used to inform clinical practice,
or referenced by the media as validated information.

Development of Design-Oriented Bond Strength Equations for FRP Bars Embedded in Concrete Exposed to Elevated Temperatures Using Explainable Machine Learning

Gia Toai Truong
Dong A University
Dinh-Nhat Truong
Ho Chi Minh City University of Architecture
Trong-Phuoc Nguyen
Ho Chi Minh City Open Universityv
Chinh Van Nguyen
The University of Danang–University of Science and Technology
Ngoc Hieu Dinh
dnhieu@dut.udn.vn

The University of Danang–University of Science and Technology

Research Article

Keywords: Machine learning, extra trees regression, whale optimization algorithm, FRP bar, bond strength, predictive model, concrete, high temperature

Posted Date: August 20th, 2026

DOI: https://doi.org/10.21203/rs.3.rs-10547278/v1

License: This work is licensed under a Creative Commons Attribution 4.0 International License.
Read Full License

Additional Declarations: No competing interests reported.

Development of Design-Oriented Bond Strength Equations for FRP Bars Embedded in Concrete Exposed to Elevated Temperatures Using Explainable Machine Learning

ABSTRACT

This study develops a hybrid Whale Optimization Algorithm–Extra Trees Regression (WOA–ETR) model to predict the bond strength of fiber-reinforced polymer (FRP) bars embedded in concrete under elevated temperatures. A database of 132 pull-out tests from the literature was used for model training and validation. The WOA was employed to optimize ETR hyperparameters, and model robustness was assessed through ten independent runs. Model interpretability was enhanced using SHapley Additive exPlanations (SHAP) and Partial Dependence Plot (PDP) analyses to clarify the effects of key variables. The proposed WOA–ETR model achieved high prediction accuracy, with an R^2 of 0.942 on the testing dataset, and outperformed benchmark machine-learning models and existing empirical equations. SHAP results showed that exposure temperature was the most influential factor, followed by surface profile, cover-to-bar diameter ratio, embedment length-to-bar diameter ratio, bar diameter, bar type, and concrete compressive strength. Guided by the interpretation results, the database was classified by embedment length and surface profile, and physically interpretable equations were derived using nonlinear least-squares regression. These equations produced nearly unbiased predictions, with mean experimental-to-predicted ratios of 1.02–1.06 and R^2 values of 0.716–0.986. Bootstrap and leave-one-out validation confirmed their robustness and parameter stability.

KEYWORDS: Machine learning; extra trees regression; whale optimization algorithm; FRP bar; bond strength; predictive model; concrete; high temperature.

INTRODUCTION

Fiber-reinforced polymer (FRP) materials offer several notable advantages for use in specialized infrastructure, including low weight, high tensile strength, strong resistance to corrosion, electrical non-conductivity, favorable fatigue behavior, and convenient handling during construction and transportation [1]. Due to these beneficial characteristics, FRP has gained significant research and engineering interest in recent years. FRP reinforcing bars, which are commonly produced through the pultrusion of fibers embedded in vinyl-ester or epoxy resin matrices, can serve as a substitute for conventional carbon-steel reinforcement in concrete structures subjected to aggressive or humid environments. As a result, FRP bars present considerable potential for enhancing the durability of structural systems [2].

In fiber-reinforced polymer-reinforced concrete (FRP-RC) structures, FRP bars are commonly manufactured using inorganic fibers such as carbon (CFRP), glass (GFRP), basalt (BFRP), and aramid (AFRP), which are embedded in a polymer resin matrix [3]. Because of the differences in material composition and casting processes, the bond interaction between FRP bars and the surrounding concrete differs significantly from that observed in conventional steel-reinforced concrete. Consequently, extensive experimental and analytical studies have been conducted to better understand this behavior. Numerous bond–slip models have been developed, and the bonding performance at ambient temperature has been widely investigated and reasonably explained [4–8].

However, the matrix phase in FRP bars typically consists of organic polymers (e.g., epoxy or vinyl ester resins), with a glass transition temperature ranging from approximately 60°C to 130°C [9]. When exposed to elevated temperatures, the resin matrix gradually transitions from a rigid glassy state to a softened or viscous state, and thermal degradation may occur [10]. This transformation significantly weakens the bond between the fibers and the surrounding matrix, leading to a reduction in the shear resistance of the FRP bars and a deterioration in their mechanical interlocking with concrete. Furthermore, several parameters can influence the degradation of bond performance in

FRP-RC systems under elevated temperatures, including the type of FRP bar, bar diameter, surface configuration, anchorage length, concrete compressive strength, and thickness of concrete cover [11–14]. Despite a number of empirical relationships have been constructed from experimental observations to describe temperature-dependent bond behavior, their applicability and predictive accuracy remain limited due to experimental constraints and complex factor interactions.

Recently, machine learning (ML) techniques have emerged as effective tools for modeling complex and nonlinear relationships between influential parameters and structural responses [15-21]. Compared with traditional experimental approaches and empirical or semi-empirical formulations, ML methods provide a cost-efficient alternative for predictive modeling. They have been successfully applied in numerous civil engineering applications, including structural health monitoring [22, 23], damage detection [24, 25], and structural performance assessment [26, 27]. By establishing direct relationships between input variables and output responses, ML models reduce the reliance on complicated mechanical formulations while often achieving improved predictive accuracy with relatively low uncertainty [28]. Consequently, a variety of ML algorithms, such as artificial neural networks (ANNs), support vector regression (SVR), random forests (RF), Gaussian process regression (GPR), and gradient boosting techniques, have been widely adopted to predict the bond behavior and structural performance of FRP-RC systems [15, 19, 29-30].

Several previous studies have demonstrated the effectiveness of ML-based models for predicting bond behavior in FRP-reinforced concrete. For example, Li et al. [31] employed nine ML models to estimate the bond strength of FRP reinforcement using a database of 557 experimental specimens. The results indicated that ANN and RF models outperform traditional empirical formulas, achieving superior prediction accuracy. Feature importance analysis further revealed that the embedment depth-to-bar diameter ratio is the most influential factor governing bond strength. Golafshani et al. [32] further developed ANN and genetic programming (GP) models based on experimental results from 159 specimens, showing that these approaches provided higher accuracy than conventional

regression models. Parametric analysis identifies key influencing variables and highlights some inconsistencies with existing design assumptions. Similarly, Basaran et al. [33] established three experimental databases containing hinged beam, end beam, and splice specimens, and applied ANN, multivariate linear regression (MLR), support vector regression (SVR), and Gaussian process regression (GPR) to estimate FRP–concrete bond strength. Among the methods, GPR showed the highest accuracy, followed by ANN, MLR, and SVR. Compared to design codes, ACI 440.1R-15 [34] provides the closest predictions but remains conservative, while other codes show limited sensitivity to test parameters.

Despite these advances, studies on predicting FRP–concrete bond strength at elevated temperatures remain limited. To the authors' knowledge, Huang et al. [35] built a backpropagation artificial neural network (BP-ANN) model based on 151 pull-out test results obtained at various temperatures. Although their model demonstrated improved predictive performance compared to existing empirical equations, further research is still needed to develop more reliable and interpretable models for FRP–concrete bond behavior at high temperatures. Using a similar database, Li et al. [36] employed multiple machine learning techniques, including backpropagation artificial neural network (BPANN), decision tree (DT), SVM, CatBoost, RF, and XGBoost, and further enhanced the dataset using a generative adversarial network (GAN). Their results showed that ML approaches can achieve high prediction accuracy, with the DT model yielding excellent performance and XGBoost demonstrating strong generalization capability. These findings highlight the potential of ML techniques while also indicating the need for further improvements in robustness and interpretability.

To address the limitations of existing empirical and ML approaches, this study proposes an integrated framework for predicting the bond strength between FRP bars and concrete under elevated-temperature conditions. A hybrid Whale Optimization Algorithm–Extra Trees Regression (WOA–ETR) model is developed, in which the Whale Optimization Algorithm is employed to

optimize the hyperparameters of the Extra Trees Regression model and enhance predictive accuracy. A comprehensive database comprising 132 experimental specimens collected from the literature is assembled for model development and validation, and the robustness of the proposed ML model is verified through repeated independent runs. To improve model interpretability and provide physical insight into the governing bond mechanisms, SHapley Additive exPlanations (SHAP) and Partial Dependence Plot (PDP) analyses are employed to quantify the influence of the input variables and investigate their effects on bond strength. Based on the knowledge extracted from these explainable artificial intelligence techniques, the experimental database is systematically classified according to embedment length and surface profile, and a series of physically interpretable predictive equations is subsequently developed using nonlinear least-squares regression. The predictive performance, robustness, and parameter stability of the developed equations are further evaluated through bootstrap resampling and leave-one-out cross-validation (LOOCV) analyses. The proposed framework therefore combines the predictive capability of advanced ML techniques, the interpretability of explainable artificial intelligent (AI), and the practicality of analytical formulations, providing both accurate prediction and engineering insight into the bond behavior of FRP bars embedded in concrete under elevated-temperature conditions.

PREPARATION OF DATABASE

Previous studies have mainly focused on the key parameters influencing the bond behavior between FRP bars and concrete subjected to high temperatures. These parameters typically include the compressive strength of concrete, the depth of concrete cover, exposure temperature, as well as the diameter and embedment length of the reinforcement bars. Nevertheless, differences in the constituent materials and manufacturing processes of FRP bars can result in significant variations in their physical and mechanical properties. In addition, variations in surface configuration can further influence the bond mechanism between FRP bars and concrete. Therefore, in addition to the

commonly considered variables, the present study also incorporates FRP-related parameters such as bar type and surface treatment method in order to provide a more comprehensive evaluation of bond performance.

The pull-out test is widely used as a conventional experimental method for assessing the bond performance between FRP bars and concrete because of its relatively simple experimental setup, short testing duration, and low cost. However, this testing approach does not fully represent the actual stress conditions experienced by reinforcement in flexural structural members. In practical structural behavior, the bond strength obtained from pull-out tests is typically higher than that observed in FRP-reinforced concrete members under service or ultimate loading conditions. Despite this limitation, pull-out testing remains a common approach for comparative investigations, especially when evaluating the influence of different surface treatments and configurations of FRP bars.

In contrast, beam-type test methods can more realistically simulate the stress state of tensile reinforcement in flexural reinforced concrete members. These tests allow stress redistribution along the beam length and introduce tensile forces to the reinforcement indirectly through flexural loading. Nevertheless, a review of the existing literature indicates that experimental studies employing beam-type specimens to examine the bond behavior between FRP bars and concrete at elevated temperatures remain relatively scarce. To overcome this limitation, the present study assembled a comprehensive experimental database consisting of 132 pull-out specimens subjected to tensile testing either during or after exposure to high temperatures, collected from previously published research [35, 36]. A schematic representation of a typical pull-out test specimen used under high-temperature conditions is shown in Fig. 1.

Table 1 summarizes the compiled experimental database. The pull-out specimens included in the dataset exhibit variations in several parameters, including: (1) the concrete compressive strength; (2) the geometric and material properties of the FRP bars, such as diameter, surface treatment, and FRP type; (3) geometric characteristics, including the concrete cover-to-bar diameter ratio and the

150 embedment length-to-bar diameter ratio; and (4) the resulting bond performance, represented by bond
151 strength. The bond strength (or average bond stress) is calculated as follows:

152 $$\tau_u = \frac{P}{\pi \times d \times l_e} \quad (1)$$

153 where τ_u denotes the bond strength (in MPa), P indicates the applied tensile forces (in N), d_b is the
154 bar diameter (in mm), and l_e refers to the embedded length (in mm).

155 Based on the experimental data collected from previous studies [35, 36], several input variables
156 were considered to evaluate the bond strength between FRP bars and concrete under high
157 temperatures. These variables include the concrete compressive strength (f'_c), FRP bar diameter (d_b),
158 concrete cover-to-FRP bar diameter ratio (c/d_b), embedded length-to-FRP bar diameter ratio (l_e/d_b),
159 type of FRP bar (*BT*), surface treatment (*ST*), and exposure temperature (*T*). The descriptive statistics
160 and distribution patterns of the target output and the associated input parameters contained in the
161 database are summarized in Table 2 and illustrated in Fig. 2, respectively.

162 Figure 2 illustrates the distributions of both input and output variables using violin plot
163 visualizations. In these plots, the width of each violin represents the relative frequency of data points
164 within a specific range, while larger nodes indicate regions with higher data density. As shown in
165 Fig. 2(a) and summarized in Table 2, the concrete compressive strength (f'_c) shows the highest
166 concentration of data between 33 and 47 MPa, with a pronounced peak around f'_c = 47 MPa. A
167 secondary but less significant concentration is observed near f'_c = 34 MPa. In contrast, only a limited
168 number of data points correspond to compressive strengths exceeding 50 MPa, suggesting that
169 experimental investigations within this range remain scarce. Overall, the distribution exhibits a
170 decreasing trend with increasing compressive strength, indicating that most specimens were tested at
171 relatively moderate strength levels.

172 The distribution of FRP bar diameter (d_b), shown in Fig. 2(b), is mainly concentrated within the
173 range of 8–10 mm. Although this range is typical for laboratory-scale experiments, it is relatively

narrow compared with empirical databases for steel reinforcement, where bar diameters generally vary between 6 and 25 mm [37]. For the concrete cover-to-bar diameter ratio (c/d_b), the values range from 3.15 to 12.5, with the majority of data concentrated between 5.75 and 7.0, as illustrated in Fig. 2(c). The relatively limited variation in concrete cover depth can be attributed to the fact that its influence on bond behavior has rarely been systematically investigated; consequently, many studies either keep this parameter constant or exclude it, particularly in standard center pull-out test configurations.

Figure 2(d) presents the distribution of the embedment length-to-bar diameter ratio (l_e/d_b). The dataset covers a wide range from 2.5 to 130.7, although most observations fall within the interval of 5.0–15.0. Regarding the exposure temperature (T), the test specimens were subjected to temperatures ranging from 20°C (room temperature) to 600°C, with the majority of data concentrated between 70°C and 200°C, as shown in Fig. 2(e) and Table 2. This trend can be explained by the temperature sensitivity of FRP materials. In particular, FRP bars incorporating polymer resins may experience softening or degradation at elevated temperatures, often beginning near the glass transition temperature, which typically lies between 60°C and 130°C [9].

To enhance data clarity and ensure its suitability for subsequent analysis, several data pre-processing procedures were performed, including data filtering, completion, and organization. First, the collected dataset was carefully screened, and records lacking essential parameters were removed prior to constructing the database. The input variables were then encoded to improve their interpretability and compatibility with the modeling process. The variables were categorized into two groups: continuous variables and categorical variables. Because ML models require numerical inputs, categorical variables were converted into numerical form through an encoding process. In this study, label encoding was adopted, whereby each category was assigned a unique integer value. As illustrated in Fig. 3, the two FRP bar types (BT), namely GFRP and BFRP, were represented by the labels 1 and 2, respectively. Furthermore, the surface configuration of FRP bars, which is an

199 important factor influencing bond performance, was also categorized and encoded. The database
200 primarily includes five surface profiles (SP): sand-coated (SC), fiber-wound (FW), ribbed bar (RB),
201 fiber-wound with sand coating (FW–SC), and ribbed bar with sand coating (RB–SC). These
202 categories were encoded using numerical labels from 1 to 5 to facilitate data processing during model
203 development. Representative examples of these surface configurations are presented in Fig. 4.
204 Figure 5 shows the distribution of these categorical variables. As indicated in Fig. 5(a), GFRP bars
205 constitute approximately 53.8% of the reinforcement types in the database, slightly exceeding the
206 proportion of BFRP bars (46.2%). Meanwhile, Fig. 5(b) demonstrates that sand-coated bars and
207 ribbed bars with sand coating represent the largest share of specimens, each accounting for 32.6% of
208 the dataset. The remaining surface configurations, including ribbed bar, fiber-wound, and fiber-
209 wound with sand coating, together comprise approximately 34.8% of the database. Due to the
210 significant variability in specimen geometry and material properties, the experimental bond strength
211 (τ_{exp}) exhibits a wide range of values, varying from 0.42 to 23.29 MPa, as summarized in Table 2 and
212 illustrated in Fig. 2(f).
213 Figure 6 presents the Pearson correlation matrix employed to assess the linear relationships
214 between the inputs and the target output. The coefficient ranges from -1.0 to 1.0, where values
215 approaching -1.0 and 1.0 indicate strong negative and positive linear relationships, respectively,
216 while values close to zero suggest weak or negligible linear associations. As illustrated in Fig. 6, the
217 correlations between the predictor variables and the bond strength vary from -0.46 to 0.39. Such
218 relatively low linear correlations indicate the complexity of the dataset and the presence of nonlinear
219 interactions among the variables, which are difficult to represent using traditional analytical
220 formulations. Therefore, ML techniques are appropriate for capturing these hidden relationships
221 within the data. The analysis indicates that the concrete compressive strength (f'_c), surface profile,
222 and FRP bar type exhibit positive correlations with bond strength, with coefficients of 0.39, 0.39,
223 and 0.34, respectively. Conversely, the embedded length-to-bar diameter ratio (l_e/b_d, P_r = -0.46) and

exposure temperature (T, P_r = -0.38) show relatively strong negative correlations with bond strength. The remaining parameters demonstrate comparatively weak correlations, suggesting a limited linear influence on the bond behavior between FRP bars and concrete after exposure to elevated temperatures.

DEVELOPMENT OF WOA-ETR MODEL

Machine learning (ML) approaches have shown considerable potential in solving various problems in structural engineering [15-30]. In this study, an ETR–WOA framework is proposed to predict the bond strength between FRP bars and concrete after exposue to elevated temperatures. The Extra Trees Regression (ETR) algorithm is employed as the primary learning model [38, 39]. For further improvement of the ETR's predictive capability, the whale optimization algorithm (WOA), recognized for its strong global search performance, is utilized to optimize the model hyperparameters [40]. This section outlines the ETR algorithm adopted in the study, followed by an introduction to the WOA method.

Extra trees regression (ETR)

The Extra Trees Regression (ETR) model, also referred to as Extremely Randomized Trees, is an ensemble learning method that combines the predictions of multiple decision trees. Unlike conventional tree-based methods, ETR introduces additional randomness by selecting both features and split thresholds randomly, which helps reduce variance and improve generalization performance. In this approach, the final prediction is obtained by averaging the outputs of all individual trees, making it particularly suitable for regression tasks. By combining multiple weak learners, ETR enhances prediction accuracy and robustness compared to single-model approaches.

As a supervised machine learning algorithm, ETR learns the relationship between input variables and target outputs from training data. Its ability to capture nonlinear relationships, handle high-

dimensional data, and model complex feature interactions makes it a powerful tool for predictive modeling in various engineering applications. A schematic representation of the ETR model is presented in Fig. 7.

The key distinction of ETR lies in its use of fully randomized split thresholds, which significantly reduces variance compared to traditional decision tree methods. In contrast to Random Forest (RF), ETR typically does not rely on bootstrap sampling, but instead uses the entire training dataset to grow each tree, which can further improve computational efficiency. This increased randomness often leads to better performance in complex and high-dimensional problems, although it may introduce a slight increase in bias.

Whale optimization algorithm (WOA)

The Whale Optimization Algorithm (WOA) as shown in Fig. 8, proposed by Mirjalili and Lewis [40], is a population-based metaheuristic inspired by the bubble-net hunting strategy of humpback whales. In WOA, each search agent represents a candidate solution, and the best solution obtained so far is considered the prey guiding the search process.

The encircling behaviour of whales is modeled as

$$D = \left| C \cdot X^{*}(t) - X(t) \right| \tag{2}$$

$$X(t+1) = X^{*}(t) - A \cdot D \tag{3}$$

where $X^{*}(t)$ is the best solution, $X(t)$ is the current whale position, and A and C are coefficient vectors defined as: $A = 2ar_1 - a$ and $C = 2r_2$, in which r_1 and r_2 are random numbers in [0, 1], and a decreases lineraly from 2 to 0 during the optimization process.

The bubble-net attacking behaviour is modeled using a spiral updating mechanism:

$$X(t+1) = D' e^{bl} \cos(2\pi l) + X^{*}(t) \tag{4}$$

where $D' = \left| X^{*}(t) - X(t) \right|$, b is a constant, and l is random number in [-1, 1]. During the search

process, the algorithm probabilistically switches between the shrinking encircling mechanism and the spiral updating strategy.

To enhance exploration, whales also move toward randomly selected individuals when $|A| \geq 1$. Through these mechanisms, WOA balances exploration and exploitation to locate the global optimum. In this study, WOA is employed to optimize the hyperparameters of the ETR model used for predicting the bond strength between FRP bar and concrete at high temperature.

Optimization of hyperparameters

To enhance the predictive capability of the extra trees regression (ETR) model, the whale optimization algorithm (WOA) was employed to determine the optimal hyperparameter configuration. Hyperparameters are predefined settings that govern the learning behavior of a model and have a significant influence on its predictive accuracy. In this study, a hybrid WOA–ETR framework was developed by integrating the WOA optimization strategy with the ETR learning algorithm. Previous studies have shown that WOA can effectively enhance the performance of hybrid machine learning models. In addition, compared with many other metaheuristic optimization algorithms, WOA requires only a small number of control parameters, making it relatively simple to implement and computationally efficient. The overall workflow of the proposed WOA–ETR framework is illustrated in Fig. 9.

The WOA algorithm was executed with a maximum of 50 iterations to search for the optimal hyperparameter combinations. To improve the robustness of the optimization process and reduce the risk of overfitting due to the limited dataset, a 5-fold cross-validation scheme was incorporated during the hyperparameter tuning stage. In this procedure, The dataset was partitioned into five folds, where each fold was iteratively used as the validation set and the remaining folds were used for model training. The optimization objective was defined as minimizing the cross-validation prediction error of the ETR model.

The search ranges for the ETR hyperparameters are listed in Table 3. These ranges were selected based on commonly recommended settings for the random forest algorithm. During the optimization process, WOA iteratively explored different hyperparameter combinations and progressively directed the search toward configurations that improved model performance. The hyperparameter tuning process considered the number of trees (*n_estimators*), tree depth limit (*max_depth*), minimum samples required for node splitting (*min_samples_split*), minimum samples at terminal nodes (*min_samples_leaf*), and the number of features evaluated per split (*max_features*). The search intervals were specified as: *n_estimators* between 200 and 1200, *max_depth* from 10 to 60, *min_samples_split* from 2 to 10, *min_samples_leaf* from 1 to 5, and *max_features* from 0.3 to 1.0.

The proposed model was implemented in Python program using several machine learning libraries. Prior to model training, all input variables were normalized using the StandardScaler function in the Scikit-learn (v1.3.2) package to eliminate the influence of different measurement units and variable scales. This procedure transforms the input data to have a mean of zero and a standard deviation of one. Subsequently, the complete dataset was then randomly split into two subsets: 70% for training and 30% for testing. The training subset was used for model construction and hyperparameter tuning, whereas the testing subset was retained for independent performance assessment.

To further assess the stability and robustness of the proposed optimization framework, the entire optimization process was repeated 10 independent times using different random seeds. For each run, WOA was employed to determine the optimal hyperparameters of the ETR model based on the cross-validation error of the training dataset. The final model obtained in each run was then retrained using the training dataset and evaluated on the testing dataset.

Evaluation metrics

The predictive performance of the proposed ML models was estimated using several statistical indicators, including the coefficient of determination (R^2), root mean square error (RMSE), mean

absolute error (MAE), and mean absolute percentage error (MAPE). A model with strong predictive capability typically exhibits an R^2 value close to 1.0, while lower values of RMSE, MAE, and MAPE indicate smaller deviations between the predicted and observed results. The mathematical expressions of these evaluation metrics are presented as follows.

$$R^2 = 1 - \frac{\sum_{i=1}^{n}\left(\tau_{e,i} - \tau_{p,i}\right)^2}{\sum_{i=1}^{n}\left(\tau_e - \overline{\tau}_e\right)^2} \tag{8}$$

$$RMSE = \sqrt{\frac{\sum_{i=1}^{n}\left(\tau_{e,i} - \tau_{p,i}\right)^2}{n}} \tag{9}$$

$$MAE = \frac{\sum_{i=1}^{n}\left(\left|\tau_{e,i} - \tau_{p,i}\right|\right)}{n} \tag{10}$$

$$MAPE = \frac{1}{n}\sum_{i=1}^{n}\left(\left|\frac{\tau_{e,i} - \tau_{p,i}}{\tau_{e,i}}\right|\right) \times 100\% \tag{11}$$

where τ_e, τ_p, $\overline{\tau}_e$, and n represent the experimental value, predicted value, mean experimental value, and total number of samples, respectively.

MODEL VERIFICATION AND DISCUSSIONS

Performance of proposed WOA-ETR model

Table 3 presents the ranges of the hyperparameters of the ETR model optimized by WOA for each independent run. Meanwhile, Table 4 summarizes the predictive performance metrics of the proposed WOA–ETR model, and Fig. 10 illustrates the corresponding boxplots of these metrics obtained with different random seeds.

The predictive performance of the proposed WOA–ETR model on the training dataset was first evaluated to assess its learning capability. Based on the average results obtained from 10 independent

runs, the model achieved a high coefficient of determination (R^2) of approximately 0.999, along with RMSE, MAE, and MAPE values of 0.091 MPa, 0.065 MPa, and 0.585%, respectively. These results indicate that the model is capable of effectively capturing the complex relationships between the input variables and the target response. As expected, the predictive performance on the training dataset is superior to that on the testing dataset. It is noted, however, that relatively higher standard deviations were observed in some training metrics, which can be attributed to the stochastic nature of the learning algorithm and variations in random data partitioning across the 10 runs.

When evaluated on the independent testing dataset obtained from 10 independent runs, the proposed WOA–ETR model achieved an average R^2 value of approximately 0.942, with corresponding RMSE, MAE, and MAPE values of 1.536 MPa, 1.067 MPa, and 16.812%, respectively. These results demonstrate that the model maintains strong predictive capability when applied to unseen data. Moreover, the relatively low standard deviations of the testing metrics indicate that the model exhibits stable and consistent performance across multiple runs. Although a decrease in performance from training to testing is observed, the difference remains within an acceptable range, suggesting that the proposed WOA–ETR model achieves good generalization ability without severe overfitting.

To further evaluate the predictive robustness of the proposed model, a leave-one-out cross-validation (LOOCV) analysis was performed using the optimized WOA–ETR model. The LOOCV yielded an R^2 value of 0.941, together with RMSE, MAE, and MAPE values of 1.521 MPa, 0.984 MPa, and 16.000%, respectively. These metrics are highly consistent with the average testing results obtained from the repeated train–test evaluations. In particular, the difference in R^2 between the testing and LOOCV results is less than 0.1%, while the corresponding error metrics remain very similar. This close agreement confirms that the predictive performance of the proposed WOA–ETR model is not strongly dependent on a particular data partition and demonstrates its excellent robustness and generalization capability.

Figure 10 presents the distribution of the evaluation metrics obtained from 10 independent runs of the proposed WOA–ETR model for both the training and testing datasets. The boxplots provide a clear visualization of the variability and stability of the model performance. As shown in the figure, the interquartile ranges of the evaluation metrics are relatively narrow for both datasets, indicating that the predictive performance of the model remains consistent across different runs. In addition, although the training dataset generally exhibits slightly better performance than the testing dataset, the difference between their metric distributions is relatively small. This observation further confirms that the proposed WOA–ETR model demonstrates stable predictive capability and good generalization performance.

Among the 10 independent runs, the best performance achieved an R^2 value of 0.944, with RMSE, MAE, and MAPE values of 1.511 MPa, 1.063 MPa, and 16.069%, respectively, for testing dataset. These results were therefore selected for further analysis of the proposed WOA–ETR model. For this best run, the optimal hyperparameters were determined as follows: n_estimators = 445.9, max_depth = 14.4, min_samples_split = 2.09, min_samples_leaf = 1.0, and max_features = 1.0 (see Table 3). Fig. 11 illustrates the convergence curve of the optimization process. As observed, the WOA–ETR model reaches its optimal performance after approximately 38 iterations, indicating that the WOA algorithm can efficiently identify suitable hyperparameter configurations within a relatively small number of iterations.

Figure 12 presents the relationship between the experimental bond strength (τ_{exp}) and the predicted values (τ_{pre}) corresponding to the best-performing model. To facilitate the assessment of prediction accuracy, three reference lines, $\tau_{pre} = \tau_{exp}$, $\tau_{pre} = 1.2\tau_{exp}$, and $\tau_{pre} = 0.8\tau_{exp}$, are incorporated. The line $\tau_{pre} = \tau_{exp}$ denotes the ideal case in which the predicted values exactly coincide with the experimental results. In general, the data points are distributed closely around this line, indicating that all models achieve a high level of predictive accuracy. For the best performance of WOA–ETR model, the

391 overall performance across the entire dataset yields a mean value of 0.99, a coefficient of variation
392 (COV) of 0.08, an R^2 of 0.986, and an RMSE of 0.737.
393
394 **Comparison with conventional ML models**
395 To evaluate the effectiveness of the proposed model, its performance was compared with several
396 conventional ML models, including RF, BR, GB, XGBoost, and ETR, over 10 independent runs
397 using multiple statistical metrics (Table 5 and Fig. 13).
398 Overall, the results confirm that ensemble-based models outperform simpler approaches; however,
399 the performance gap among advanced models is relatively narrow. RF and BR exhibit similar
400 predictive capability, both achieving testing R^2 values of 0.895, but with relatively high error levels
401 (RMSE ≈ 2.06 MPa and MAPE ≈ 36%), indicating limited generalization ability and reduced
402 suitability for precise prediction tasks.
403 Boosting-based models (GB and XGBoost) show clear improvement, with testing R^2 values of
404 0.934 and 0.938, respectively, and substantially reduced errors. Nevertheless, the extremely high
405 training performance of XGBoost (R^2 = 1.000) raises concerns regarding overfitting, particularly in
406 the absence of external validation. This suggests that the model may be capturing noise or dataset-
407 specific patterns rather than robust underlying relationships.
408 The ETR model provides competitive performance, achieving a testing R^2 of 0.936 with relatively
409 low error metrics (RMSE = 1.605 MPa and MAPE = 17.26%). While this supports the robustness of
410 ETR, its perfect training performance (R^2 = 1.000 with zero error) is also indicative of potential
411 overfitting, despite its inherent randomness. This behavior warrants further scrutiny, particularly
412 regarding dataset size and complexity.
413 The proposed WOA-ETR model achieves the highest testing R^2 (0.942) and the lowest error
414 values (RMSE = 1.536 MPa, MAE = 1.067 MPa, and MAPE = 16.81%). Although the improvement

over the standalone ETR model is relatively small (e.g., $\Delta R^2 \approx 0.006$ and $\Delta RMSE \approx 0.07$ MPa), it is consistent across all evaluation metrics, indicating a reliable enhancement in predictive performance. Moreover, WOA-ETR exhibits slightly lower standard deviations compared to the standalone ETR model, suggesting improved stability and consistency across multiple runs. While the differences are modest, they demonstrate the ability of the optimization process to enhance the robustness of the base model.

In terms of predictive capability, WOA-ETR consistently outperforms ETR across all evaluation metrics. This consistent improvement highlights the effectiveness of integrating WOA in refining model performance and producing more reliable predictions. In addition, both ETR and WOA-ETR achieve very high training accuracy, reflecting strong learning capability. The corresponding testing results remain stable and competitive, indicating that the models maintain good generalization performance.

In summary, the WOA-ETR model provides the best overall performance among the evaluated models, offering a balanced improvement in both accuracy and stability. The results suggest that metaheuristic optimization can further refine high-performing ensemble models, even when the baseline performance is already strong. Further validation on independent datasets would help confirm the broader applicability of the proposed approach.

EXISTING DESIGN METHODS

Due to the complex mechanisms governing bond deterioration in FRP-concrete under elevated temperatures, most existing studies have primarily reported qualitative observations, while only a limited number of predictive mathematical models have been developed. Previous research consistently indicates that bond strength decreases as temperature increases. For instance, Lu et al. [41] observed a reduction in the bond strength between GFRP bars and concrete with rising temperature, with the degradation tending to stabilize beyond approximately 110^{o}C. They also noted

that although higher concrete compressive strength enhances bond performance, this improvement becomes marginal when the strength exceeds 30 MPa. Similarly, Katz et al. [42], through pull-out tests conducted at various temperatures, reported a temperature-dependent decline in bond strength, with different rates of reduction across temperature ranges. The most significant degradation occurs within the glass transition temperature range (80–120°C). At around 125°C, bond strength drops to approximately 50% of its room-temperature value, and further decreases to only 10–20% when the temperature exceeds 200°C. Wang et al. [43] further investigated the degradation behavior over a wider temperature range (20–350°C), confirming the progressive reduction in bond capacity.

Experimental work by El-Gamal [13] on 39 GFRP-reinforced concrete specimens subjected to high temperatures revealed that all specimens failed in shear. The results demonstrated that bond strength diminishes with both increasing temperature and exposure duration. Specifically, exposure to 100°C and 200°C for 3 hours resulted in a reduction of about 20%, while exposure to 350°C for 2 hours and 3 hours led to a significant decrease of approximately 50%. Based on these findings, modified formulations derived from ACI 440.1R-06 [44] and CEB-FIP [45] guidelines were proposed to predict bond strength at elevated temperatures. In addition, Ozkal et al. [11] compared the high-temperature behavior of GFRP-reinforced and steel-reinforced concrete, showing that bond degradation in both systems follows an approximately linear trend with increasing temperature. They also proposed an empirical design equation for predicting bond strength in GFRP-concrete at elevated temperatures, which demonstrated good agreement with test results. A summary of the existing interfacial bond models for FRP-concrete at high temperatures is provided in Table 6.

The calculated results obtained from the existing mathematical models, together with the test data reported in the literature [11] and [13], and the predictions generated by the WOA–ETR model, are illustrated in Fig. 14 for comparative analysis. As observed across the three experimental datasets, the WOA–ETR predictions exhibit a similar variation trend to both the analytical model outputs and the experimental measurements within each group.

A quantitative assessment of the prediction performance of the WOA–ETR model and the existing mathematical formulations, based on the ratio (τ_{exp}/τ_{pre}), is presented in Table 7. For the dataset reported by El-Gamal et al. [13], the conventional analytical models show slightly lower accuracy compared to the WOA–ETR approach. This can be attributed to the fact that these models were developed from limited experimental conditions, considering only a few influencing factors such as concrete compressive strength, exposure time, and the temperature difference between testing and ambient conditions. As indicated in Table 7, although the mean values of the predictions are similar, the WOA–ETR model achieves notable improvements in performance metrics, with reductions in COV (68.0%) and RMSE (58.9%), as well as an increase in R^2 (15.2%).

In contrast, the mathematical model proposed by Ozkal et al. [11] exhibits slightly better predictive accuracy, mainly because it was specifically calibrated using its corresponding experimental dataset. Nevertheless, such models generally rely on predefined input parameters and are valid only within the scope of the original experimental conditions, thereby limiting their broader applicability. On the other hand, despite a marginal reduction in precision, the WOA–ETR model provides enhanced adaptability and generalization capability. When trained on a sufficiently large and representative dataset, it can effectively predict interfacial bond strength under a wide range of conditions while still satisfying practical engineering accuracy requirements.

GLOBAL INTERPRETATION OF BOND STRENGTH PREDICTION

SHAP summary investigation

The SHAP-based analysis of the WOA–ETR model provides a comprehensive understanding of the contribution of each input variable to the prediction of bond strength. As illustrated in Fig. 15(a), feature importance is quantified using the mean absolute SHAP values calculated from the testing dataset, revealing clear differences in the influence of the input parameters. Among all variables, the exposure temperature (T) is identified as the most significant factor, with the highest average SHAP

value of approximately 2.15. The surface profile (*SP*) also demonstrates a substantial contribution, with a mean SHAP value close to 2.08, indicating a comparable level of importance to temperature.

The concrete cover-to-bar diameter ratio (c/d_b) is shown to be an important parameter, which aligns with its physical role in enhancing confinement around reinforcing bars and resisting pull-out failure. Similarly, the embedment length-to-bar diameter ratio (l_e/d_b) exhibits a notable contribution, reflecting its influence on mechanical interlocking and stress transfer along the bar–concrete interface. In contrast, bar diameter (d_b), bar type (*BT*), and concrete compressive strength (f'_c) present relatively low SHAP values, suggesting a limited impact on the model predictions. This observation is somewhat different from findings in previous studies, where concrtee compressive strength has often been considered a key parameter [34, 45].

Figure 15(b) presents the SHAP summary plot, which offers further insight into the effects of individual variables on the model output. In this plot, the horizontal axis represents SHAP values, while the input variables are arranged vertically in descending order of importance. Each data point corresponds to an individual sample, and its color (ranging from blue to red) indicates the relative magnitude of the feature value. The spread of points along the horizontal axis reflects the extent and direction of each variable's influence on the predicted bond strength. For example, data points associated with higher exposure temperatures (*T*) are predominantly located on the negative SHAP side, indicating that increasing temperature generally leads to a reduction in the predicted bond strength of FRP bar–concrete systems after thermal exposure, with an approximate decrease of up to 10 units. In addition to identifying the relative importance of variables, the SHAP summary plot also reveals their directional effects. Higher values of surface profile (*SP*), concrete cover ratio (c/d_b), bar type (*BT*), and compressive strength (f'_c) tend to contribute positively to bond strength. Conversely, larger values of bar diameter (d_b) and embedment length ratio (l_e/d_b) are generally associated with negative SHAP values, suggesting a reduction in bonding capacity.

Overall, these findings provide a detailed and physically meaningful interpretation of the factors

influencing FRP bar–concrete bond behavior under elevated temperature conditions, while also highlighting the key variables governing the predictive performance of the WOA–ETR model.

Partial dependence plots (PDPs) investigation

To further investigate the influence of individual variables on bond strength, partial dependence plots (PDPs) were generated for all input parameters. The PDPs reveal the average marginal effect of each variable while accounting for the influence of the remaining predictors. As shown in Fig. 16(a), temperature exhibits a pronounced nonlinear influence on bond strength. A rapid reduction is observed between ambient temperature and approximately 350°C, indicating progressive deterioration of the FRP–concrete bond system. This degradation can be attributed to resin softening and decomposition, thermal incompatibility between the FRP bar and surrounding concrete, and the gradual deterioration of concrete mechanical properties under elevated temperatures. Beyond approximately 350°C, the PDP curve approaches a plateau, suggesting that the majority of bond degradation has already occurred and further temperature increases have only a limited influence on the residual bond strength.

The PDP of bar diameter, shown in Fig. 16(d), reveals a relatively weak influence on bond strength compared with temperature and embedment ratio. A gradual reduction in bond strength is observed as the diameter increases from 6 to approximately 10 mm, which can be attributed to less uniform stress transfer and increased radial stresses at the FRP–concrete interface. Beyond this range, the influence of diameter becomes negligible, indicating that bond performance is increasingly governed by temperature and surface characteristics rather than bar diameter itself.

The PDP analysis further reveals a nonlinear influence of embedment ratio on bond strength, as illustrated in Fig. 16(e). A relatively stable response is observed at low embedment ratios, followed by a region of significant reduction and finally a plateau at large embedment ratios. These distinct response regions suggest that a single global equation may not adequately represent the bond

behavior over the entire embedment-length range. Therefore, separate predictive equations were subsequently developed for short-, intermediate-, and long-embedment regimes to better capture the underlying bond mechanisms and reduce prediction uncertainty.

Meanwhile, Fig. 16(b) indicates that GFRP and BFRP bars exhibit comparable bond-strength responses under elevated temperatures, suggesting that bar type exerts a relatively limited influence compared with temperature and surface characteristics. In contrast, surface profile (SP), shown in Fig. 16(c), exhibits a more pronounced effect on bond performance. The results indicate that mechanically interlocked surfaces generally provide superior bond resistance compared with solely coated surfaces. Based on the PDP results, the effectiveness of the investigated surface profiles in enhancing bond strength can be ranked as follows: sand-coated (SC), ribbed (RB), fiber wound and sand coated (SC-FW), and sand-coated and ribbed (RB-SC).

Concrete compressive strength, illustrated in Fig. 16(f), also exhibits a positive influence on bond strength. The PDP remains relatively flat for concrete strengths below approximately 40 MPa and increases progressively thereafter, indicating that the beneficial contribution of concrete strength becomes more pronounced at higher strength levels. This behavior is consistent with the enhanced confinement and improved mechanical properties provided by higher-strength concrete. Similarly, the concrete cover-to-bar diameter ratio (c/d_b) shown in Fig. 16(g) exhibits a positive influence on bond strength. Increasing concrete cover enhances confinement around the embedded FRP bar and delays splitting-related failures. However, the relatively small slope of the PDP curve indicates that the influence of (c/d_b) is less significant than those of temperature and embedment ratio.

Overall, the PDP analysis demonstrates that temperature is the dominant factor governing bond degradation of FRP bars embedded in concrete under elevated temperatures, followed by embedment ratio and surface profile. In contrast, bar diameter, concrete cover ratio, and bar type exhibit comparatively weaker influences. Furthermore, the nonlinear response observed for the embedment ratio provides strong evidence that different bond mechanisms govern short-, intermediate-, and long-

565 embedment specimens, thereby supporting the development of separate predictive equations for the
566 three embedment-length regimes.
567
568 **DEVELOPMENT OF PREDICTIVE EQUATIONS**
569 Although the global interpretation and PDP analyses provided valuable insights into the factors
570 governing the bond strength of FRP-concrete exposed to elevated temperatures, the development of
571 a single unified design equation remained challenging due to the heterogeneous nature of the
572 experimental database. To identify the governing parameters, a WOA-ETR model was first
573 developed using the entire database, and SHAP analysis was subsequently employed to quantify the
574 relative importance of the input variables. The results indicated that temperature, surface profile, bar
575 type, and embedment ratio (l_e/d_b) were among the most influential parameters affecting bond strength.
576 Although the embedment ratio was not identified as the dominant predictor, both the experimental
577 observations [4, 35] and PDP analysis revealed that specimens with different embedment ratios
578 exhibited substantially different bond-strength responses. In particular, the relationship between bond
579 strength and embedment ratio was characterized by three distinct response regions, consisting of an
580 initial stable region at low embedment ratios, a transition region associated with a significant
581 reduction in bond strength, and a plateau region at large embedment ratios. These observations
582 suggest that different bond-transfer mechanisms govern the behavior of short-, intermediate-, and
583 long-embedment specimens and that a single global equation may not adequately represent the entire
584 database.
585 To account for the observed differences in bond behavior while maintaining physical
586 interpretability, a hierarchical modeling framework was adopted. The database was first classified
587 according to the embedment ratio, which governs the stress-transfer mechanism between the FRP bar
588 and the surrounding concrete. Subsequently, additional classifications based on surface profile and
589 bar type were considered for the short-embedment specimens, where the highest variability in bond

strength was observed. The collected data for each case are presented in detail in Table 8. Separate predictive equations were then developed for each subgroup using nonlinear regression analysis. The proposed framework aims to improve prediction accuracy while preserving the simplicity required for practical engineering applications.

Rationale for database classification

Although the WOA-ETR model demonstrated excellent predictive performance, its black-box nature limits direct application in engineering design. Therefore, a set of simplified predictive equations was developed based on the insights obtained from the SHAP and PDP analyses. The SHAP results identified temperature, surface profile, and embedment ratio as important parameters governing the bond strength of FRP bars exposed to elevated temperatures. Furthermore, the PDP analysis revealed a nonlinear influence of the embedment ratio (l_e/d_b), characterized by three distinct response regions corresponding to short-, intermediate-, and long-embedment conditions. These observations suggest that different bond-transfer mechanisms govern the bond behavior within different embedment-length ranges.

To improve prediction accuracy while maintaining physical interpretability, the experimental database was classified into three embedment-length regimes based on the trends identified from the PDP analysis, as illustrated in Fig. 17:

Case 1: $l_e/d_b \leq 20$;

Case 2: $20 < l_e/d_b \leq 80$; and

Case 3: $l_e/d_b > 80$.

These ranges correspond to short-, intermediate-, and long-embedment conditions, respectively. Accordingly, 106, 15, and 11 specimens were included in the short-, intermediate-, and long-embedment groups, respectively. The proposed classification is also consistent with the mechanics of bond stress transfer. For short embedment lengths, bond stresses are distributed relatively

615 uniformly along the bonded region, and failure is primarily governed by local interfacial mechanisms.
616 As the embedment length increases, bond stresses become progressively more non-uniform, resulting
617 in a reduction in the average bond strength and a transition toward different stress-transfer
618 mechanisms [4, 47]. The effectiveness of the proposed classification was evidenced by the reduced
619 prediction scatter observed for the intermediate- and long-embedment groups.

620 The short-embedment database ($l_e/d_b \leq 20$) exhibited substantially larger prediction scatter than
621 the remaining datasets, indicating that additional factors influenced the bond response within this
622 regime. The SHAP analysis revealed that surface profile was among the most influential variables
623 for Case 1 specimens. Moreover, different surface configurations mobilize distinct bond-transfer
624 mechanisms, including frictional resistance, mechanical interlocking, and bearing action [47-49].
625 Therefore, an additional classification based on surface profile was introduced for the short-
626 embedment database to further reduce prediction variability and facilitate the development of
627 physically interpretable predictive equations.

628

629 **Development of predictive equations**

630 The SHAP and PDP analyses revealed that the governing mechanisms of bond strength vary
631 considerably with embedment length and surface configuration. Consequently, the development of a
632 single unified predictive equation was found to be inadequate for accurately representing the entire
633 experimental database. To address this limitation, a hierarchical framework was adopted in which
634 the database was first classified according to embedment ratio and subsequently subdivided
635 according to surface profile for short-embedment specimens. Separate predictive equations were then
636 established using nonlinear regression analysis for each subgroup. This approach enables the
637 derivation of physically interpretable design equations while preserving an acceptable level of
638 prediction accuracy.

To facilitate practical implementation, a unified mathematical framework was adopted for all predictive equations. The bond strength was expressed as a multiplicative function of the governing parameters, including c/d_b, l_e/d_b, f'_c, d_b, and T, identified through the SHAP and PDP analyses:

$$\tau_u = \alpha \left(\frac{c}{d_b} \right)^{\beta} \left(\frac{l_e}{d_b} \right)^{\gamma} f_c'^{\varepsilon} d_b^{\delta} e^{\theta T} \tag{12}$$

where α, β, γ, ε, δ, and θ are regression coefficients determined separately for each subgroup. Depending on the embedment-length regime and surface configuration (i.e., Case 1), some variables were excluded when their influence was found to be insignificant.

Predictive equations for short-embedment lengths ($l_e/d_b \leq 20$)

As discussed previously, an additional classification based on surface profile was introduced to further reduce prediction variability and facilitate the development of physically interpretable predictive equations. Accordingly, the database corresponding to Case 1 was subdivided into four groups according to the FRP bar surface profile: (i) sand-coated bars (SP = 1), (ii) fiber-wound bars (SP = 2), (iii) ribbed bars (SP = 3), and (iv) ribbed bars with sand coating (SP = 5). The resulting subdatasets contained 34, 9, 20, and 43 specimens, respectively. The fiber-wound FRP bars with sand coating (SP = 4) category contained only one specimen. Therefore, the available data were insufficient for regression analysis, and no predictive equation was developed for this surface profile.

To derive the predictive equations, a nonlinear least-squares regression approach was employed to determine the optimal values of the model coefficients, namely α, β, γ, ε, δ, and θ. The objective of this procedure was to minimize the discrepancy between the predicted bond strengths and the corresponding experimental measurements. Preliminary regression analyses indicated that the optimal values of α, β, γ, ε, δ, and θ differed substantially among the surface-profile groups, suggesting distinct bond-transfer mechanisms. Therefore, separate predictive equations were established for each surface profile.

For sand-coated FRP bars (SP = 1): Since the variables l_e/d_b and f'_c remained constant within this subdataset, their effects were excluded from the regression analysis. The resulting predictive equation is expressed as follows:

$$\tau_u = 8.22\left(\frac{c}{d_b}\right)^{0.32} d_b^{0.26} e^{-0.012T} \quad (13)$$

For fiber-wound bars (SP = 2): Since all variables except temperature remained constant within this subdataset, temperature was identified as the sole governing parameter influencing bond strength. Consequently, the predictive equation was formulated exclusively as a function of temperature. The resulting predictive equation is expressed as follows:

$$\tau_u = 2.9e^{-0.005T} \quad (14)$$

For ribbed bar (SP = 3): Since the variables d_b remained constant within this subdataset, its effect was excluded from the regression analysis. The resulting predictive equation is expressed as follows:

$$\tau_u = 0.47\left(\frac{c}{d_b}\right)^{0.78} f_c'^{0.48} e^{-0.002T} \quad (15)$$

For ribbed bars with sand coating (SP = 5): The resulting predictive equation is expressed as follows:

$$\tau_u = 1.29 d_b^{-0.37}\left(\frac{c}{d_b}\right)^{0.18}\left(\frac{l_e}{d_b}\right)^{-0.11} f_c'^{0.86} e^{-0.0018T} \quad (16)$$

Predictive equations for intermediate-embedment lengths ($20 < l_e/d_b \leq 80$)

For the intermediate-embedment regime ($20 < l_e/d_b \leq 80$), the database was analyzed as a single group because further subdivision did not provide sufficient data for reliable regression. The resulting predictive equation is given by:

$$\tau_u = 26.6 d_b^{1.3}\left(\frac{c}{d_b}\right)^{-0.05}\left(\frac{l_e}{d_b}\right)^{-0.97} f_c'^{0.04} e^{-0.002T} \quad (17)$$

Predictive equations for long-embedment lengths (l_e/d_b > 80)

For the long-embedment regime (l_e/d_b > 80), regression analysis showed that d_b and c/d_b remained constant throughout the dataset. Consequently, these variables were excluded from the predictive model. The resulting equation is expressed as follows:

$$\tau_u = 301.6\left(\frac{l_e}{d_b}\right)^{-1} f_c'^{0.002} e^{-0.0016T} \quad (18)$$

Verification of the proposed predictive equations

The predictive performance of the proposed equations was assessed by comparing the predicted bond strengths with the corresponding experimental measurements. Fig. 18 presents the relationship between the predicted and experimental values, whereas Table 9 summarizes the statistical indicators of the developed equations for the various embedment-length regimes and surface profiles. Overall, the equations demonstrated satisfactory predictive capability, with the mean values of $\tau_{u,\exp}/\tau_{u,\text{pre}}$ ranging from 1.02 to 1.06. Since all mean values are close to unity, the developed equations can be considered essentially unbiased and capable of providing reliable estimates of bond strength. The slightly greater-than-one values indicate a minor tendency toward conservative predictions, whereby the predicted bond strengths are marginally lower than the corresponding experimental values.

For the short-embedment regime ($l_e/d_b \leq 20$), the prediction accuracy varied depending on the surface profile of the FRP bars. The equation developed for sand-coated FRP bars (SP = 1) achieved an R^2 value of 0.851, indicating a strong correlation between predicted and measured bond strengths (Fig. 18(a)). However, the corresponding COV of 0.320 was the highest among all developed equations, suggesting relatively large variability in the prediction errors. This observation implies that although the proposed equation successfully captured the general trend of the experimental data, additional factors influencing bond behavior may not have been fully represented by the simplified

model. For fiber-wound FRP bars (SP = 2, Fig. 18(b)), the predictive equation yielded an R^2 value of 0.861 and a substantially lower COV of 0.196, demonstrating improved consistency of prediction. The ribbed FRP bars (SP = 3, Fig. 18(c)) exhibited a slightly lower coefficient of determination (R^2 = 0.768) and a COV of 0.203, indicating moderate predictive accuracy. Meanwhile, the equation developed for ribbed FRP bars with sand coating (SP = 5, Fig. 18(d)) produced the lowest scatter among the short-embedment groups, with a COV of 0.118, although the corresponding R^2 value was 0.716. The reduced scatter suggests that the dominant bond mechanisms associated with this surface configuration were effectively captured by the proposed formulation.

The equations developed for the intermediate-embedment ($20 < l_e/d_b \leq 80$, Fig. 18(e)) and long-embedment ($l_e/d_b > 80$, Fig. 18(f)) regimes exhibited substantially improved predictive performance. Equation (17), corresponding to the intermediate-embedment regime, achieved an R^2 value of 0.986 and a COV of only 0.064, indicating excellent agreement with the experimental observations and very limited prediction variability. Similarly, Eq. (18) for the long-embedment regime produced an R^2 value of 0.969 and the lowest COV among all cases (0.032), demonstrating highly consistent predictive performance. These results suggest that the governing bond mechanisms become more stable and predictable as the embedment length increases, allowing the simplified equations to more effectively represent the bond-strength behavior.

To further evaluate the reliability of the developed equations, bootstrap resampling and leave-one-out cross-validation (LOOCV) analyses were conducted. Table 10 summarizes the predictive robustness and parameter stability results. Overall, the LOOCV results remained reasonably consistent with the calibration performance, confirming the generalization capability of the proposed equations. The strongest robustness was observed for the intermediate- and long-embedment regimes, where the reductions in R^2 were limited to only 0.005 (from 0.993 to 0.988) and 0.014 (from 0.974 to 0.960), respectively. Similarly, the equation developed for ribbed FRP bars with sand coating (SP = 5) maintained satisfactory predictive performance, with the R^2 value decreasing from 0.842 to 0.777

under LOOCV validation. In contrast, larger reductions in predictive accuracy were observed for SP = 1 ($\Delta R^2 = 0.047$), SP = 2 ($\Delta R^2 = 0.137$), and SP = 3 ($\Delta R^2 = 0.094$), indicating greater sensitivity to the exclusion of individual specimens and reflecting the influence of the limited sample sizes and inherent variability within these sub-databases.

The bootstrap and LOOCV analyses also provided valuable insights into the stability of the fitted coefficients. The equations developed for SP = 2 and the long-embedment regime exhibited excellent parameter stability, with the maximum coefficient of variation (CV) among the fitted parameters remaining below approximately 10%. Likewise, most coefficients in the SP = 5 and intermediate-embedment equations were found to be highly stable, with the exception of one parameter exhibiting moderate variability (CV ≈ 33% and 37%, respectively). Conversely, the SP = 1 and SP = 3 equations showed substantially larger parameter uncertainty, with maximum parameter CV values exceeding 50% and several bootstrap confidence intervals crossing zero. These findings suggest that certain parameter effects in these equations are not uniquely identified by the available experimental data. Nevertheless, the corresponding equations still achieved acceptable predictive performance, with calibration R^2 values of 0.862 and 0.811 and LOOCV R^2 values of 0.815 and 0.717 for SP = 1 and SP = 3, respectively. Therefore, these equations may still be considered suitable empirical predictive tools within the investigated parameter ranges, although their coefficients should be interpreted with greater caution than those of the more robust formulations.

In general, the proposed classification framework based on embedment length and surface profile successfully reduced the variability within the experimental database and enabled the development of physically interpretable predictive equations. The consistently high R^2 values, mean prediction ratios close to unity, and generally satisfactory LOOCV performance confirm the effectiveness of the proposed methodology. The additional bootstrap and LOOCV analyses further demonstrated that the reliability of the developed equations depends on both the sample size and the complexity of the underlying bond mechanisms. The equations developed for the intermediate- and long-embedment

758 regimes, as well as for SP = 5, exhibited excellent predictive robustness and parameter stability,
759 whereas the equations for SP = 1 and SP = 3 showed greater parameter uncertainty despite
760 maintaining acceptable prediction accuracy. Nevertheless, it should be noted that the intermediate-
761 and long-embedment datasets contained only 15 and 11 specimens, respectively. Additional
762 experimental data would therefore be beneficial to further confirm the long-term robustness and
763 general applicability of the proposed equations over a wider range of conditions.
764
765 **CONCLUSIONS**
766 This study investigated the bond strength between FRP bars and concrete at elevated temperatures
767 using both machine-learning and analytical approaches. A hybrid WOA–ETR model was developed
768 to predict bond strength, and physically interpretable predictive equations were subsequently derived
769 based on insights obtained from the machine-learning analyses. The main findings of this study are
770 summarized as follows:
771 - The proposed WOA–ETR model demonstrated stable and reliable performance across ten
772 independent runs, achieving an R^2 of 0.942, along with RMSE, MAE, and MAPE values of 1.536
773 MPa, 1.067 MPa, and 16.812%, respectively, on the testing dataset.
774 - In comparison with other machine learning approaches, including RF, BR, GB, XGBoost, and
775 the conventional ETR model, the WOA–ETR consistently yielded superior predictive accuracy. This
776 improvement highlights the effectiveness of the whale optimization algorithm in fine-tuning ETR
777 hyperparameters.
778 - When benchmarked against existing empirical formulations derived from experimental studies
779 reported in the literature, the proposed model incorporates a broader range of influencing variables
780 and demonstrates greater adaptability to diverse datasets. Consequently, it offers enhanced predictive
781 accuracy and generalization capability compared to traditional approaches.

- SHAP and PDP analyses identified exposure temperature (T) as the most influential parameter affecting bond strength, followed by surface profile (SP), concrete cover-to-bar diameter ratio (c/d_b), embedment length-to-bar diameter ratio (l_e/d_b), bar diameter (d_b), bar type (BT), and concrete compressive strength (f'_c). Furthermore, the interpretation analyses revealed that the governing bond mechanisms vary significantly with embedment length and surface profile, highlighting the complex interactions among the influencing variables.

- Based on the insights obtained from the machine-learning interpretation analyses, the experimental database was classified according to embedment length and surface profile, and a series of physically interpretable predictive equations was developed using nonlinear least-squares regression. The proposed equations provided nearly unbiased predictions, with mean values of $\tau_{u,\mathrm{exp}}/\tau_{u,\mathrm{pre}}$ ranging from 1.02 to 1.06. The equations also exhibited satisfactory predictive performance, with R^2 values ranging from 0.716 to 0.986 and coefficients of variation between 0.032 and 0.320.

- While the WOA–ETR model functions as a black-box predictor, the proposed equations provide a transparent and computationally efficient alternative for engineering applications. The integration of ML interpretation techniques with simplified analytical formulations offers both high predictive accuracy and practical applicability for estimating the bond strength of FRP bars embedded in concrete at elevated temperatures.

- Bootstrap and leave-one-out cross-validation (LOOCV) analyses confirmed the predictive robustness and stability of the SHAP/PDP-guided equations. The most reliable formulations were obtained for the intermediate- and long-embedment regimes, as well as for ribbed FRP bars with sand coating, where both predictive accuracy and parameter stability were consistently maintained. The robustness assessment further revealed that the reliability of the fitted coefficients depends on the size and variability of the corresponding sub-database, highlighting the importance of uncertainty quantification when developing empirical bond-strength equations from limited experimental datasets. Overall, the robustness analyses provide additional confidence that the proposed equations

807 can serve as practical design-oriented tools while retaining a clear physical interpretation of the
808 governing bond mechanisms.

809 Although the proposed equations demonstrated satisfactory to excellent predictive performance,
810 the available database remains limited for certain embedment-length regimes and surface-profile
811 categories. Therefore, additional experimental data are recommended to further validate and refine
812 the developed formulations and to extend their applicability to a broader range of conditions.

813

814 **REFERENCES**

815 [1] Truong GT, Choi K-K. Effect of short multi-walled carbon nanotubes on the mode I fracture
816 toughness of woven carbon fiber reinforced polymer composites. Construction and Building
817 Materials 2020; 259: 119696. https://doi.org/10.1016/j.conbuildmat.2020.119696.
818 [2] Beauchemin S, Fournier B, Duchesne J. Durability of FRP bars and FRP-reinforced concrete
819 beams: A critical review of accelerated aging tests and performance insights. Composites Part
820 B: Engineering 2026; 308: 112965.
821 [3] Edah GO, Atiba JO, Fayomi OSI. Advancements in fibre-reinforced polymers: Properties,
822 applications (A mini review). Next Materials 2025; 8: 100743.
823 [4] Liao JJ, Zeng JJ, Bai YL, Zhang L. Bond strength of GFRP bars to high strength and ultra-high
824 strength fiber reinforced seawater sea-sand concrete (SSC). Composite Structures 2022; 281;
825 115013.
826 [5] Xiong Z, Zeng Y, Li LG, Kwan AKH, He SH. Experimental study on the effects of glass fibres
827 and expansive agent on the bond behaviour of glass/basalt FRP bars in seawater sea-sand
828 concrete. Construction and Building Materials 2021; 274: 122100.
829 [6] Pan R, Zou J, Liao Peng, Dong S, Deng J. Effects of fiber content and concrete cover on the
830 local bond behavior of helically ribbed GFRP bar and UHPC. Journal of Building Engineering
831 2023; 80: 107939.
832 [7] Godat A, Aldaweela S, Aljaberi H, Al Tamimi N, Alghafri E. Bond strength of FRP bars in
833 recycled-aggregate concrete. Construction and Building Materials 2021; 267: 120919.
834 [8] Quayyum S. Bond behaviour of fibre reinforced polymer (FRP) rebars in concrete. Master Thesis,
835 The University Of British Columbia, Canada; 2010.
836 [9] Kashwani GA, Al-Tamimi AK. Evaluation of FRP bars performance under high temperature.
837 Physics Procedia 2014; 55: 296–300.

[10] Bai Yu, Vall´ee T, Keller T. Modeling of thermal responses for FRP composites under elevated and high temperatures. Composites Science and Technology 2008; 68(1): 47–56.
[11] Özkal FM, Polat M, Yagan M, Öztürk MO. Mechanical properties and bond strength degradation of GFRP and steel rebars at elevated temperatures. Construction and Building Materials 2018; 184: 45–57.
[12] Solyom S, Di Benedetti M, Guadagnini M, Balazs GL. Effect of temperature on the bond behaviour of GFRP bars in concrete. Composite Part B 2020; 183: 107602.
[13] El-Gamal S. Bond strength of glass fiber-reinforced polymer bars in concrete after exposure to elevated temperatures. Journal of Reinforced Plastics and Composites 2014; 33(23): 2151-2163.
[14] McIntyre ERE, Bisby L, Stratford T. Bond strength of frp reinforcement in concrete at elevated temperature. In *7th international Conference on Fiber Reinforced Polymer (FRP) Composites in Civil Engineering (CICE 2014),* Vancouver, Canada; 2014.
[15] Truong GT, Nguyen TP, Truong D-N, Dinh NH. Shear strength assessment of FRP-reinforced concrete beams without shear reinforcement: database-driven approach and prediction models. Magazine of Concrete Research 2026; 78(1-2): 18-44.
[16] Truong GT, Roh Y-S, Nguyen T-P, Dinh NH. In-plane lateral strength prediction of unreinforced masonry walls subjected to lateral loads using optimized boosting algorithms. Structures 2025; 80: 110025.
[17] Truong D-N, To V-L, Truong GT, Jang H-S. Engineering punching shear strength of flat slabs predicted by nature-inspired metaheuristic optimized regression system. Frontiers of Structural and Civil Engineering 2024; 18: 551-567.
[18] Ho TN-T, Nguyen T-P, Truong GT. Concrete spalling identification and fire resistance prediction for fired RC columns using machine learning-based approaches. Fire Technology 2024; 60: 1823-1866.
[19] Truong GT, Choi K-K, Kim CS. Assessment of punching shear strength of FRP-RC slab-column connections using machine learning algorithms. Engineering Structures 2022; 255: 113898.
[20] Tran V-L, Kim J-K. Ensemble machine learning-based models for estimating the transfer length of strands in PSC beams. Expert Systems With Applications 2023; 221: 119768.
[21] Cascardi A, Micelli F, Aiello MA. An Artificial Neural Networks model for the prediction of the compressive strength of FRP-confined concrete circular columns. Engineering Structures 2017; 140: 199-208.
[22] Bader A, Shtayat A, Al-Mistarehi B. Enhancing structural health monitoring with AI-ML algorithms: A focus on crack detection and prediction. Asian Journal of Civil Engineering 2025; 26: 1907-1918.

[23] Shibu M, Kumar KP, Pillai VJ, Murthy H, Chandra S. Structural health monitoring using AI and ML based multimodal sensors data. Measurement: Sensors 2023; 27: 100762.
[24] Huynh T-C, Hoang N-D, Pham Q-Q, Truong GT, Nguyen T-T. Electromechanical admittance-based automatic damage assessment in plate structures via one-dimensional CNN-based deep learning models. Frontiers of Structural and Civil Engineering 2024; 18: 1730-1751.
[25] Dang N-L, Phan N-T-V, Hoang N-D, Truong M-P, Pham Q-Q, Kim J-T, Truong GT, Huynh T-C. Enhancement of PZT-based damage detection in real-scale post-tensioned anchorage under ambient conditions. Journal of Constructional Steel Research 2024; 220: 108841.
[26] Truong GT, Choi K-K, Kim C-S. Implementation of boosting algorithms for prediction of punching shear strength of RC column footings. Structures 2022; 46: 521-538.
[27] Dai Y, Roy K, Fang Z, Chen B, Raftery GM, Lim JBP. A novel machine learning model to predict the moment capacity of cold-formed steel channel beams with edge-stiffened and un-stiffened web holes. Journal of Building Engineering 2022; 53: 104592.
[28] Ji H, Tian Y, Fu C, Ye H. Transfer learning enables prediction of steel corrosion in concrete under natural environments. Cement and Concrete Composites 2024; 148: 105488.
[29] Cakiroglu C, Islam K, Bekda G, Kim S, Geem ZW. Interpretable machine learning algorithms to predict the axial capacity of FRP-reinforced concrete columns. Materials 2022; 15(8): 2742.
[30] AlHamaydeh M, Markou G, Bakas N, Papadrakakis M. AI-based shear capacity of FRP-reinforced concrete deep beams without stirrups. Engineering Structures 2022; 264: 114441.
[31] Li Z, Qi J, Hu Y, Wang J. Estimation of bond strength between UHPC and reinforcing bars using machine learning approaches. Engineering Structures 2022; 262: 114311.
[32] Golafshani E, Rahai A, Sebt M. Artificial neural network and genetic programming for predicting the bond strength of GFRP bars in concrete. Materials and Structures 2015; 48: 1581–1602.
[33] Basaran B, Kalkan I, Bergil E, Erdal E. Estimation of the FRPconcrete bond strength with code formulations and machine learning algorithms. Composite Structures **268**, 113972 (2021).
[34] ACI 440.1R-15. Guide for the Design and Construction of Structural Concrete Reinforced with Fiber-Reinforced Polymer (FRP) Bars, ACI Committee 440, 2015.
[35] Huang L, Chen J, Tan X. BP-ANN based bond strength prediction for FRP reinforced concrete at high temperature. Engineering Structures 2022; 257: 114062.
[36] Li S, Gao Y, Wang B, Li J, Yu Y. Machine learning based predictive model for bond strength of FRP reinforced concrete at high temperature. AIP Advances 2025; 15: 025125.

[37] Heng Liu, Yanhai Liu, Aijun Li, Lei H. Experimental study on the bond performance of deformed steel bar in ultrahigh performance concrete. Case Studies in Construction Materials 2023; 18: e01874.
[38] https://scikit-learn.org/stable/modules/generated/sklearn.tree.ExtraTreeRegressor.html
[39] Sudhamathi T, Perumal K. Ensemble regression based Extra Tree Regressor for hybrid crop yield prediction system. Measurement: Sensors 2024; 35: 101277.
[40] Mirjalili S, Lewis A. The Whale Optimization Algorithm. Advances in Engineering Software 2016; 95: 51-67.
[41] Lu XL, Zhou CD, Jin Y. Test study on bond behavior between GFRP bar and concrete in high temperature. Journal of Building Structures 2007; 28(5): 32–39.
[42] Katz A, Berman N, Bank LC. Effect of high temperature on bond strength of FRP rebars. Journal of Composites for Construction 1999; 3(2): 73–81.
[43] Wang XL, Zha XX, Zhang XC. Bond behavior of FRP rebar and concrete at elevated temperature. Journal of Harbin Institute of Technology 2013; 45(06): 8–15.
[44] ACI 440.1R-06. Guide for the Design and Construction of Structural Concrete Reinforced with Fiber-Reinforced Polymer (FRP) Bars, ACI Committee 440, 2006.
[45] fib Model Code for Concrete Structures 2010, International Federation for Structural Concrete (fib), Lausanne, Switzerland, 2013.
[46] ACI 440.11-22. Building Code Requirements for Structural Concrete Reinforced with Glass FiberReinforced Polymer (GFRP) Bars - Code and Commentary, ACI Committee 440, 2022.
[47] Basaran B, Kalkan I. Investigation on variables affecting bond strength between FRP reinforcing bar and concrete by modified hinged beam tests. Composite Structures 2020; 242: 112185.
[48] Jiang K, Wang X, Ben Q, Ding L, Chen Z, Liew JYR, Du H, Wu Z. Bond behavior of BFRP bars in ultra-high performance seawater sea-sand concrete reinforced by non-metallic fibers. Engneering Structures 2024; 318: 118699.
[49] He N, Chen Z, Tang J, Zhao Y, Liang Y, Zhou J. Experimental study on bond behavior of CFRP bars in coral sea-sand seawater concrete. Structures 2025; 79: 109526.
[50] Hamad RJA, Megat Johari MA, Haddad RH. Mechanical properties and bond characteristics of different fiber reinforced polymer rebars at elevated temperatures. Constr Build Mater 2017; 142: 521-535.
[51] Wang YL. Experimental study on tensile property of FRP bars and bond behavior between FRP bars and concrete after high temperature. Zhengzhou University; 2013

TABLES AND FIGURES

List of Tables:

Table 1. Database of pullout test specimens under high temperature.

Table 2. Descriptive statistics of the compiled database used in this study.

Table 3. Optimal hyperparameter configurations of the ETR model used in this study.

Table 4. Performance of the WOA–ETR model over 10 independent runs.

Table 5. Model performance averaged across 10 independent executions.

Table 6. Overview of bond strength formulations for FRP-reinforced concrete under high temperatures.

Table 7. Comparison of predictive accuracy of different models.

Table 8. Detailed experimental database for each case.

Table 9. Predictive performance of proposed equations.

Table 10. Robustness assessment of the proposed equations using LOOCV and parameter stability analysis.

Table 1. Database of pullout test specimens under high temperature.

Reference	No. of specimens	T (°C)	BT*	SP**	d_b (mm)	l_e/d_b	c/d_b	f'_c (MPa)	τ_{exp} (MPa)
Wang et al. [43]	34	20-300	1-2	1	9.5-12.7	5.0	3.15-7.37	33.7	1.5-21.5
Lu et al. [41]	18	70-230	1	4	6.0	21.0-130.7	12.5	36.3-50. 7	1.86-15.67
El-Gamal [13]	13	25-350	1	3	8.0	5.0	12.0	52.31-62.94	9.15-19.04
Ozkal et al. [11]	9	23-600	1	1	9.0	50.0	10.56	40.0	3.38-9.94
Hamad et al. [50]	8	23-375	1-2	1-2	10.0	10.0	7.0	40.0	0.42-8.34
Wang [51]	50	20-350	1-2	3-5	6.0-10.0	2.5-20.0	4.60-8.88	32.0-58.9	2.02-23.29

Note:
f'_c = concrete compressive strength; d_b = FRP bar diameter; c/d_b = concrete cover to FRP bar diameter; l_e/d_b = bonded length to FRP bar diameter;
SP = surface profile; BT = type of FRP bar; τ_{exp} = average bond strength (or bond strength) obtained from experimental results.
* 1 = glass FRP, and 2 = basalt FRP
** 1 = sand-coated (SC), 2 = fiber-wound (FW), 3 = ribbed bar (RB), 4 = fiber-wound with sand coating (FW-SC), and 5 = ribbed bar with sand coating (RB-SC).

Table 2. Descriptive statistics of the compiled database used in this study.

Parameters	Description	Unit	Min.	$Q_{0.25}$	$Q_{0.5}$	$Q_{0.75}$	Max.	Mean	SD	Type
f'_c	Concrete compressive strength	MPa	32.0	33.7	46.9	46.9	62.9	43.33	8.06	Input
d_b	Bar diameter	mm	6.0	8.0	8.0	9.5	12.7	8.62	1.73	Input
c/d_b	Concrete cover-to-bar diameter ratio	-	3.15	5.75	7.0	10.56	12.5	7.15	2.89	Input
l_e/d_b	Embeded length-to-bar diameter ratio	-	2.5	5.0	5.0	15	133.7	19.64	30.59	Input
SP	Surface profile	-	1	-	-	-	5	-	-	Input
BT	Bar type	-	1	-	-	-	2	-	-	Input
T	Temperature	ºC	20	70	150	220	600	158.4	109.2	Input
τ_{exp}	Bond strength	MPa	0.42	3.24	10.5	15.53	23.29	10.0	6.31	Output

Note: Min. = Minimum; Max. = Maximum; SD = Standard deviation; $Q_{0.25}$ = 0.25 quantile (or 25 percentile); $Q_{0.5}$ = 0.5 quantile (or 50 percentile); $Q_{0.75}$ = 0.75 quantile (or 75 percentile)

Table 3. Optimal hyperparameter configurations of the ETR model used in this study.

ML models	Hyperparameters	Ranges of values	Optimal values*										Default values
			1	2	3	4	5	6	7	8	9	10	
Extra trees regression (ETR)	n_estimators	[200,…,1200]	230.2	734.6	445.9	200	262.3	908.4	210.1	806.1	1087.0	229.4	100
	max_depth	[10,…,60]	11.5	13.8	14.4	10.0	11.4	12.5	12.3	11.8	11.7	10.5	None
	min_samples_split	[2,…,10]	2.46	2.81	2.09	2.0	2.46	2.49	2.03	2.44	2.34	2.10	2
	min_samples_leaf	[1,…,5]	1.15	1.50	1.0	1.0	1.14	1.40	1.01	1.36	1.17	1.05	1
	max_features	[0.3,…,1.0]	1.0	1.0	1.0	1.0	1.0	0.96	1.0	0.99	0.89	1.0	1.0

* Using WOA technique

Table 4. Performance of the WOA–ETR model over 10 independent runs.

Run	Training				Testing			
	R^2	RMSE (MPa)	MAE (MPa)	MAPE (%)	R^2	RMSE (MPa)	MAE (MPa)	MAPE (%)
1	0.999	0.027	0.01	0.089	0.941	1.542	1.081	16.167
2	0.995	0.420	0.290	3.406	0.939	1.576	1.08	17.680
3	0.999	0.003	0.001	0.00	0.944	1.511	1.063	16.069
4	0.999	0.143	0.079	0.801	0.942	1.533	1.059	16.095
5	0.999	0.068	0.033	0.313	0.943	1.527	1.062	16.127
6	0.999	0.028	0.013	0.122	0.942	1.529	1.057	17.863
7	0.999	0.026	0.01	0.089	0.942	1.54	1.076	16.134
8	0.999	0.027	0.126	0.119	0.943	1.521	1.053	17.863
9	0.999	0.029	0.013	0.123	0.941	1.544	1.069	18.036
10	0.999	0.141	0.077	0.792	0.941	1.541	1.067	16.090
Mean	**0.999**	**0.091**	**0.065**	**0.585**	**0.942**	**1.536**	**1.067**	**16.812**
SD	**0.001**	**0.119**	**0.084**	**0.980**	**0.001**	**0.017**	**0.009**	**0.860**

Table 5. Model performance averaged across 10 independent executions.

Models	Training								Testing							
	R^2	SD	RMSE (MPa)	SD	MAE (MPa)	SD	MAPE (%)	SD	R^2	SD	RMSE (MPa)	SD	MAE (MPa)	SD	MAPE (%)	SD
RF	0.971	0.002	1.056	0.038	0.669	0.015	15.07	0.89	0.895	0.005	2.060	0.052	1.555	0.051	36.04	2.69
BR	0.971	0.002	1.058	0.036	0.669	0.019	15.08	0.86	0.895	0.006	2.062	0.055	1.565	0.044	36.16	2.66
GB	0.997	0.000	0.356	0.014	0.286	0.012	4.96	0.27	0.934	0.010	1.634	0.123	1.177	0.096	21.56	1.82
XGBoost	1.000	0.000	0.024	0.006	0.016	0.004	0.26	0.06	0.938	0.011	1.583	0.147	1.164	0.113	22.79	3.77
ETR	1.000	0.000	0.000	0.000	0.000	0.000	0.0	0.00	0.936	0.005	1.605	0.063	1.119	0.046	17.26	0.56
WOA-ETR	0.999	0.001	0.091	0.119	0.065	0.084	0.585	0.98	0.942	0.001	1.536	0.017	1.067	0.009	16.812	0.86

Table 6. Overview of bond strength formulations for FRP-reinforced concrete under high temperatures.

References	Formulas
El-Gamal et al. [13]	$\tau_{re,ACI} = 20.23\frac{\sqrt{f_c'}}{d_b} - 0.015\Delta T\sqrt{t}$ $\tau_{re,FIP} = 2.5\sqrt{f_c'} - 0.015\Delta T\sqrt{t}$ τ_{re} = bond strength at any temperature, f'_c = concrete compressive strength, d_b = FRP bar diameter, ΔT = difference between test and room temperatures, and t = exposure duration of specimens at high temperature.
Ozkal et al. [11]	$\tau_{m,T} = \gamma_m \eta_m f(T)$ with 23°C ≤ T ≤ 600°C $\gamma_g = \frac{\tau_{g,23}}{\tau_{s,23}}$, $\eta_g = \frac{1473 - T}{1450}$, $f(T) = 0.981\tau_{s,23}\left(1 - \frac{T}{1450}\right)$ $\tau_{g,23}$ and $\tau_{s,23}$ = peak bond stresses of GFRP and ordinary steel reinforcements at 23°C, γ_g = bond strength coefficient of GFRP, η_g = thermal brittlenness coefficient of GFRP bar, $f(T)$ = thermal behavior function.

Table 7. Comparison of predictive accuracy of different models.

Data	Models	τ_{exp}/τ_{pre}			
		Mean	COV	R^2	RMSE (MPa)
El-Gamal's study	ACI 440.1R-06	0.99	0.09	0.834	1.246
	CEB-FIP	1.01	0.09	0.833	1.238
	WOA-ETR	0.99	0.03	0.960	0.511
Ozkal et al.'s study	Ozkal et al.	1.01	0.04	0.979	0.282
	WOA-ETR	1.00	0.08	0.900	0.883

Table 8. Detailed experimental database for each case.

Data classification		No. of specimens	T (°C)	BT	SP	d_b (mm)	l_e/d_b	c/d_b	f'_c (MPa)	τ_{exp} (MPa)
$l_e/d_b \leq 20$	SP = 1	34	20-300	1-2	1	9.5-12.7	5	3.15-7.37	33.7	1.5-21.5
	SP = 2	9	23-325	1-2	2	10	10	7	40	0.42-2.63
	SP = 3	20	20-350	1	3	8	5	5.75-12	46.9-62.93	2.65-19.04
	SP = 5	43	20-270	2	5	6-10	2.5-20	4.6-8.88	32-58.9	9.12-23.29
$20 < l_e/d_b \leq 80$		15	23-600	1	1-4	6-9	50-79.7	10.56-12.5	40-50.67	3.24-9.94
$l_e/d_b > 80$		11	110-230	1	4	6	85-130.7	12.5	36.27-50.67	1.86-2.95

Table 9. Predictive performance of proposed equations.

Data		No. of specimens	Equations	$\tau_{u,exp}/\tau_{u,pre}$		
				Mean	COV	R^2
$l_e/d_b \leq 20$	SP = 1	34	Eq. (13)	1.05	0.320	0.851
	SP = 2	9	Eq. (14)	1.02	0.196	0.861
	SP = 3	20	Eq. (15)	1.02	0.203	0.768
	SP = 5	43	Eq. (16)	1.05	0.118	0.716
$20 < l_e/d_b \leq 80$		15	Eq. (17)	1.02	0.064	0.986
$l_e/d_b > 80$		11	Eq. (18)	1.06	0.032	0.969

Table 10. Robustness assessment of the proposed equations using LOOCV and parameter stability analysis.

Data		No. of specimens	Calibration R^2	LOOCV R^2	ΔR^2	Maximum parameter COV (%)	Assessment
$l_e/d_b \leq 20$	SP = 1	34	0.862	0.815	0.047	54.8	Moderate
	SP = 2	9	0.873	0.736	0.137	7.1	Good
	SP = 3	20	0.811	0.717	0.094	52.1	Moderate
	SP = 5	43	0.842	0.777	0.065	32.7	Good
$20 < l_e/d_b \leq 80$		15	0.993	0.988	0.005	36.8	Excellent
$l_e/d_b > 80$		11	0.974	0.960	0.014	10.2	Excellent

List of Figures:

Fig. 1. Schematical configuration of a typical pull-out test specimen exposed to high temperature.

Fig. 2. Statistical distributions of the study's input and output variables.

Fig. 3. Two main types of FRP bars used in this study.

Fig. 4. Details of surface profile configurations of FRP bars.

Fig. 5. Distribution of categorical variables.

Fig. 6. Correlation between input and output variables.

Fig. 7. Flowchart of extra trees regression (ETR) algorithm.

Fig. 8. Schematic representation of the bubble-net hunting mechanism in the whale optimization algorithm (WOA).

Fig. 9. Model framework used in this study.

Fig. 10. Boxplots of the evaluation metrics obtained from ten independent runs of the proposed WOA–ETR model for the training and testing datasets.

Fig. 11. Convergence curve of the WOA optimization process corresponding to the best-performing WOA–ETR model.

Fig. 12. Predictions by the best WOA-ETR model in comparison with experimental results.

Fig. 13. Comparison of predictive performance of different ML models.

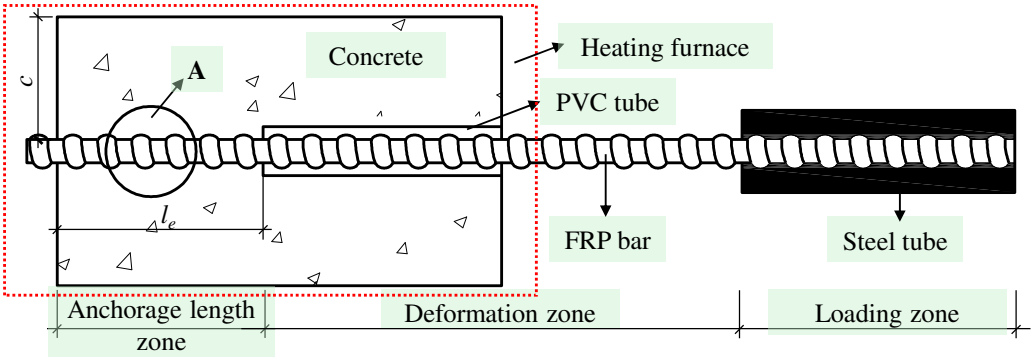
Fig. 14. Comparison of bond strength predicted by WOA-ETR and mathematical models with experimental results.

Fig. 15. Global interpretation of bond strength predictions using the best-performing WOA–ETR model.

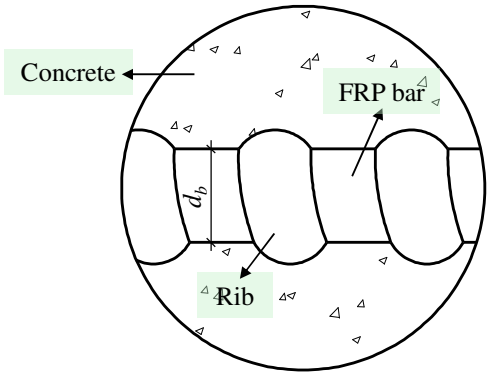
Fig. 16. Partial dependence plots of bond strength predictions using the best-performing WOA–ETR model.

Fig. 17. Classification of the experimental database according to embedment length based on PDP analysis.

Fig. 18. Comparison of the proposed equation predictions with experimental results.



(a) Schematic of a pull-out test specimen



(b) Detail A

Fig. 1. Schematical configuration of a typical pull-out test specimen exposed to high temperature.

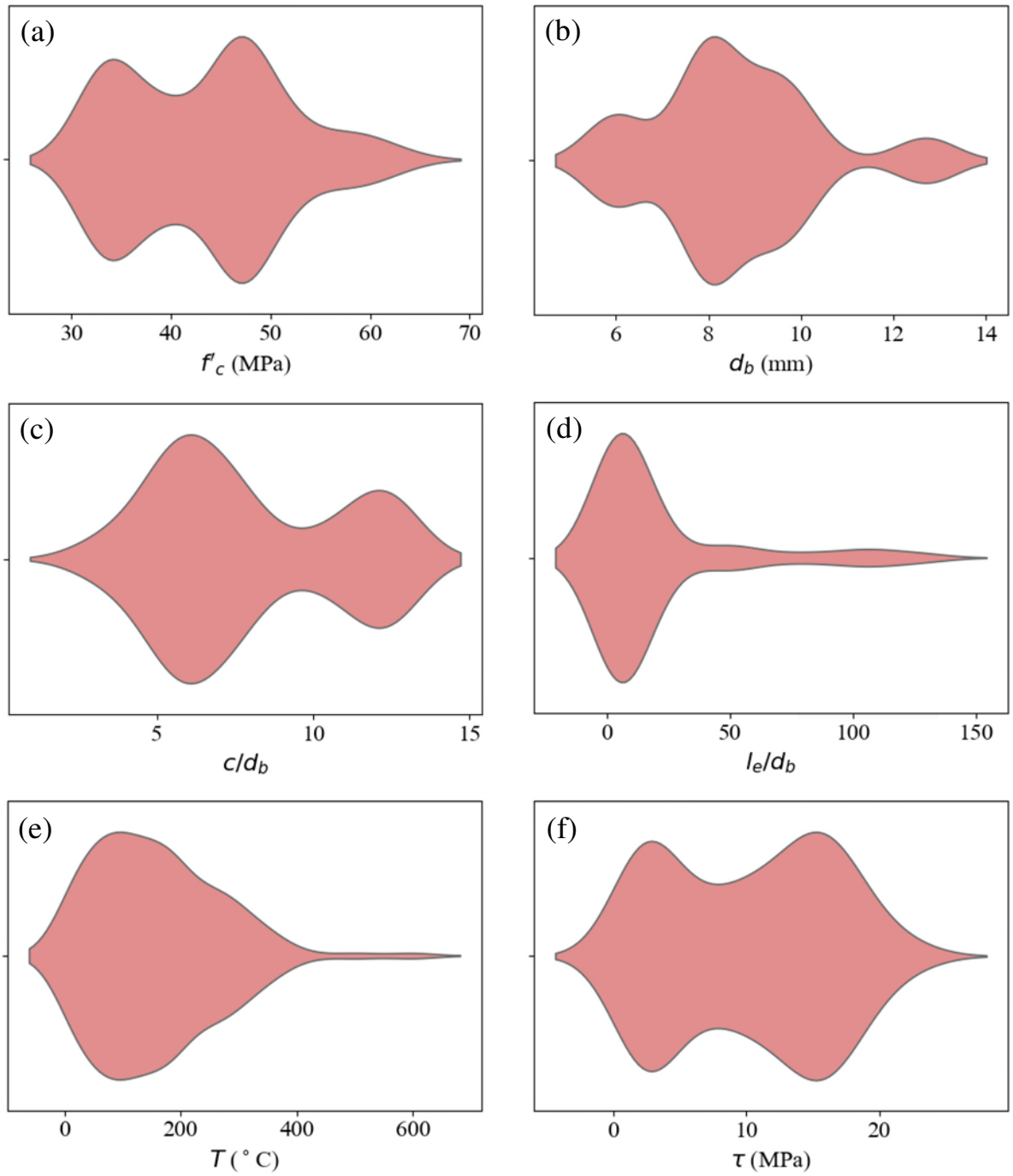


Fig. 2. Statistical distributions of the study's input and output variables.



(a) GFRP (b) BFRP

Fig. 3. Two main types of FRP bars used in this study.

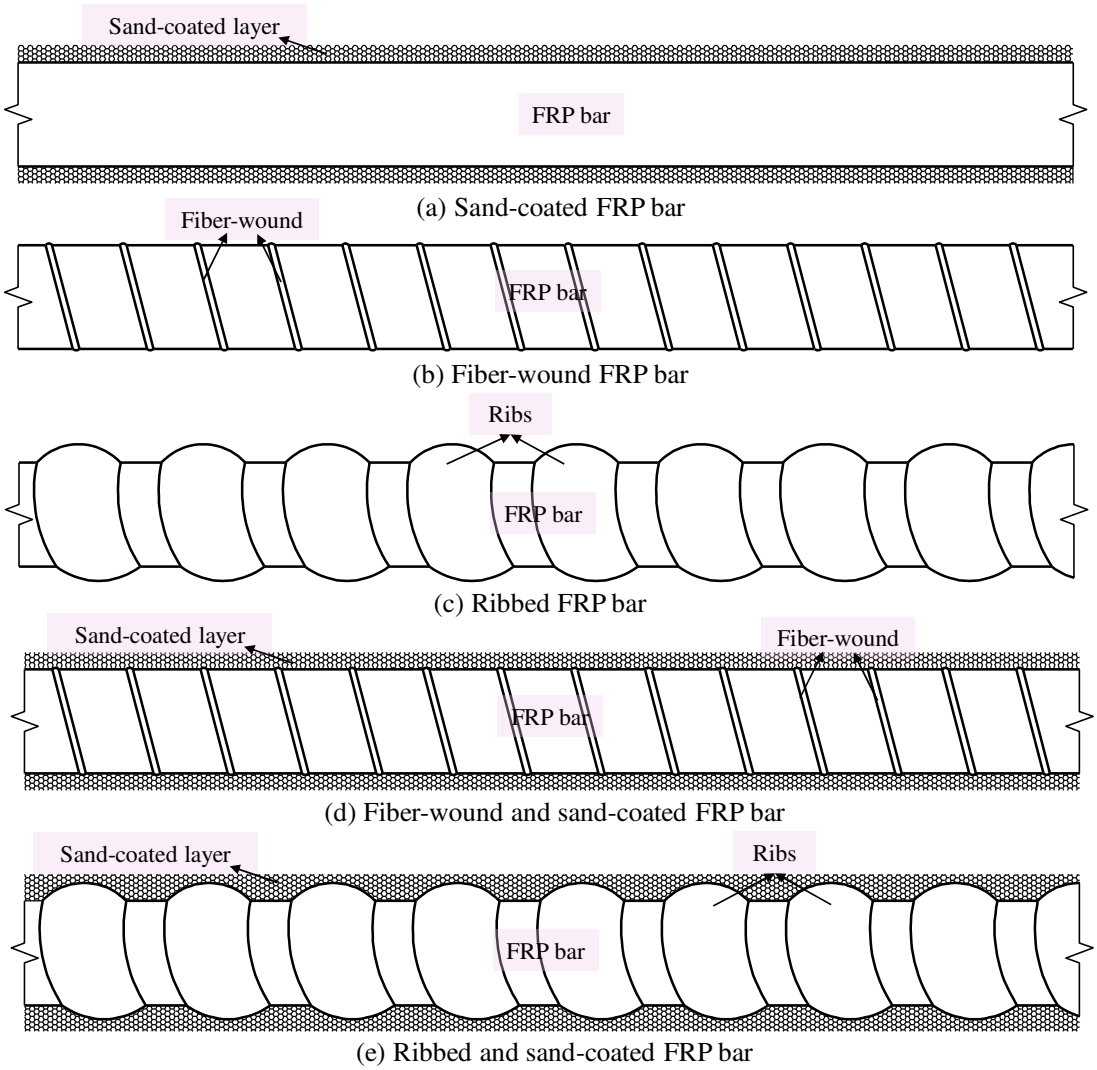
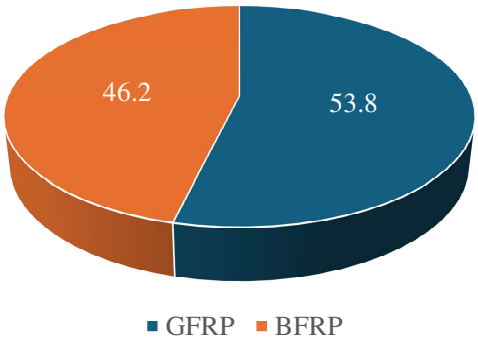
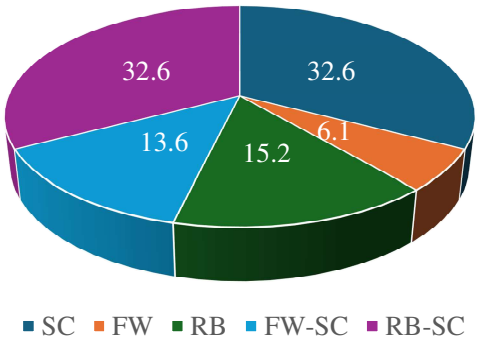


Fig. 4. Details of surface profile configurations of FRP bars.



GFRP: Glass fiber reinforced polymer
BFRP: Basalt fiber reinforced polymer

(a) FRP bar type



SC: Sand-coated; FW: Fiber-wound; RB: Ribbed bar
FW-SC: Fiber-wound with sand coating
RB-SC: ribbed bar with sand coating

(b) Surface profile

Fig. 5. Distribution of categorical variables.

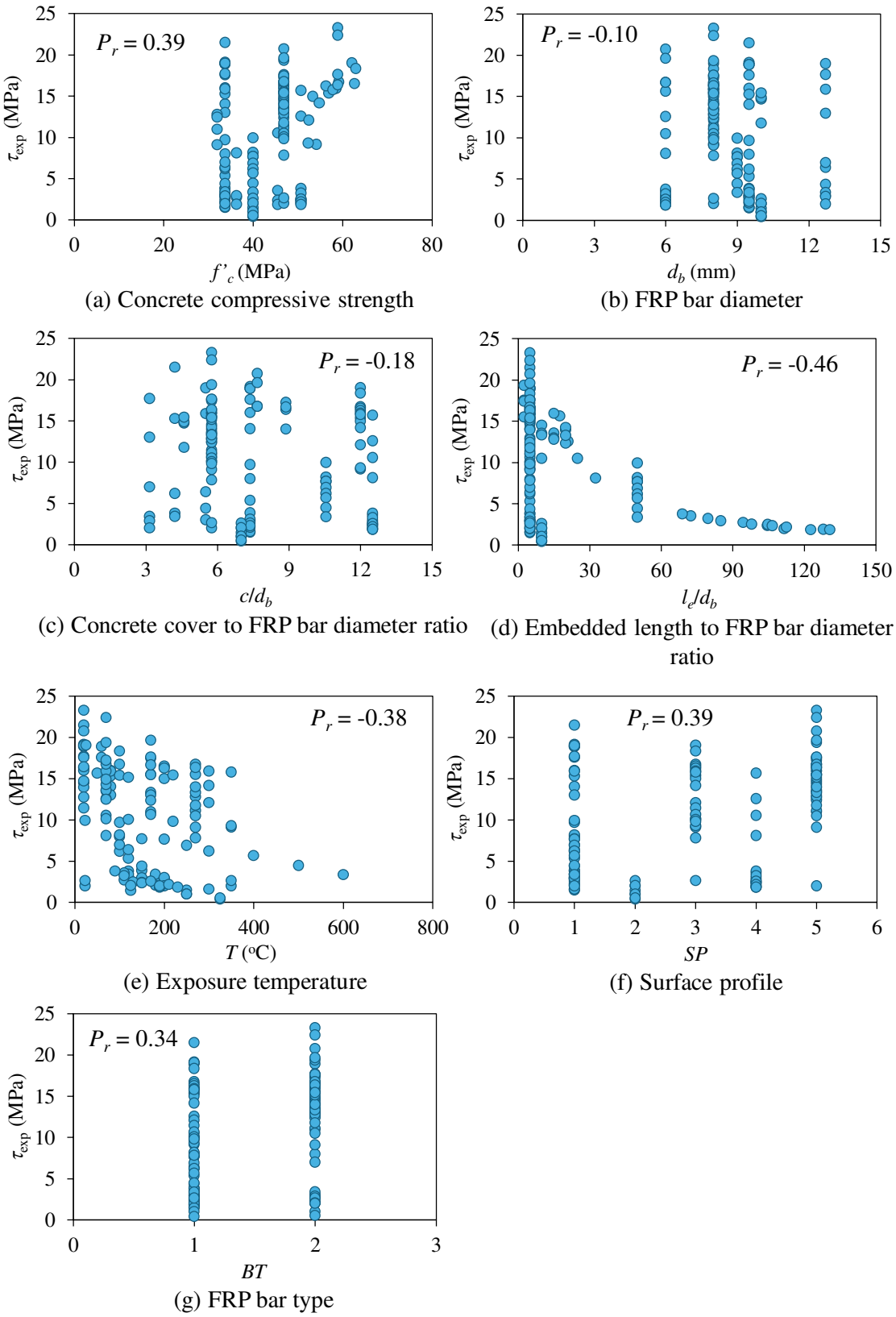


Fig. 6. Correlation between input and output variables.

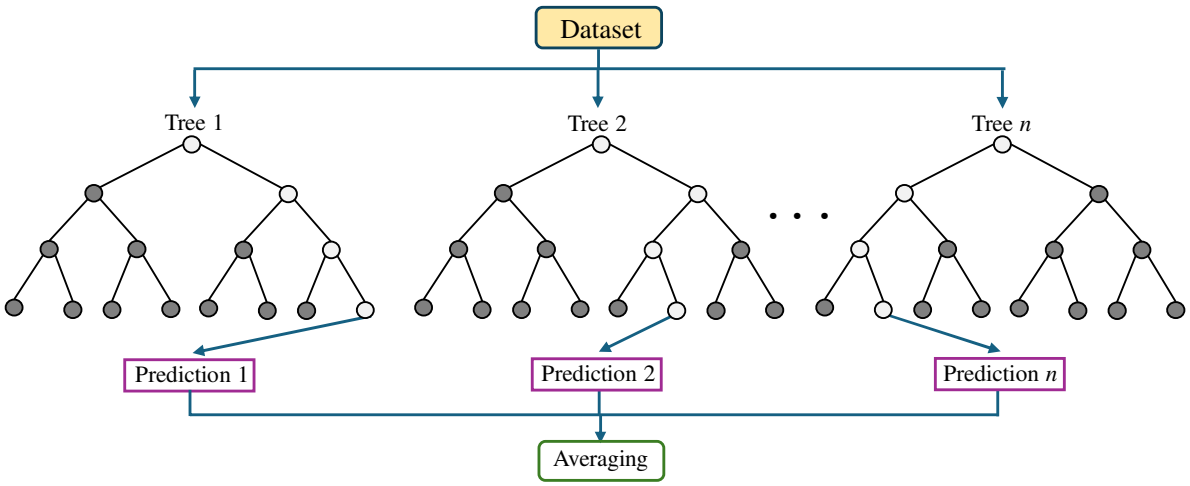


Fig. 7. Flowchart of extra trees regression (ETR) algorithm.

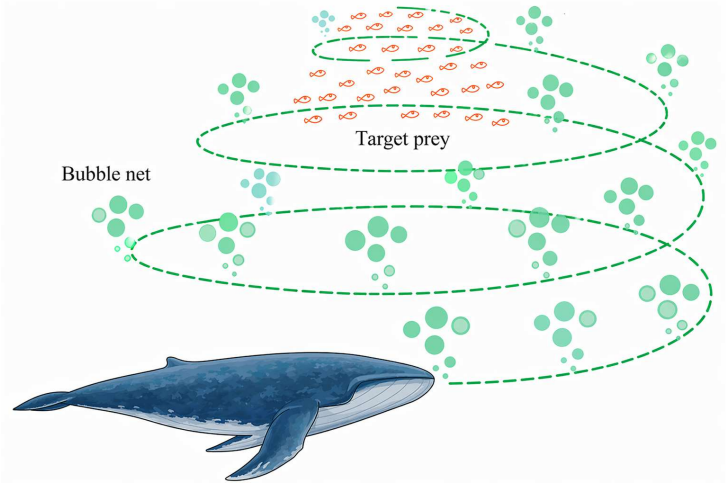


Fig. 8. Schematic representation of the bubble-net hunting mechanism in the whale optimization algorithm (WOA).

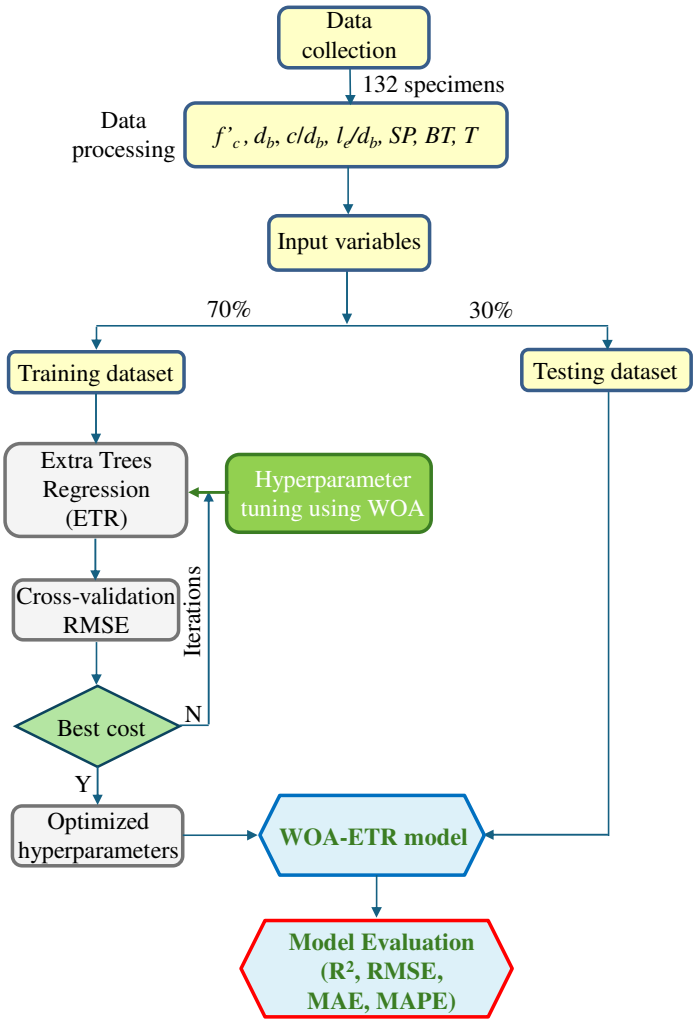
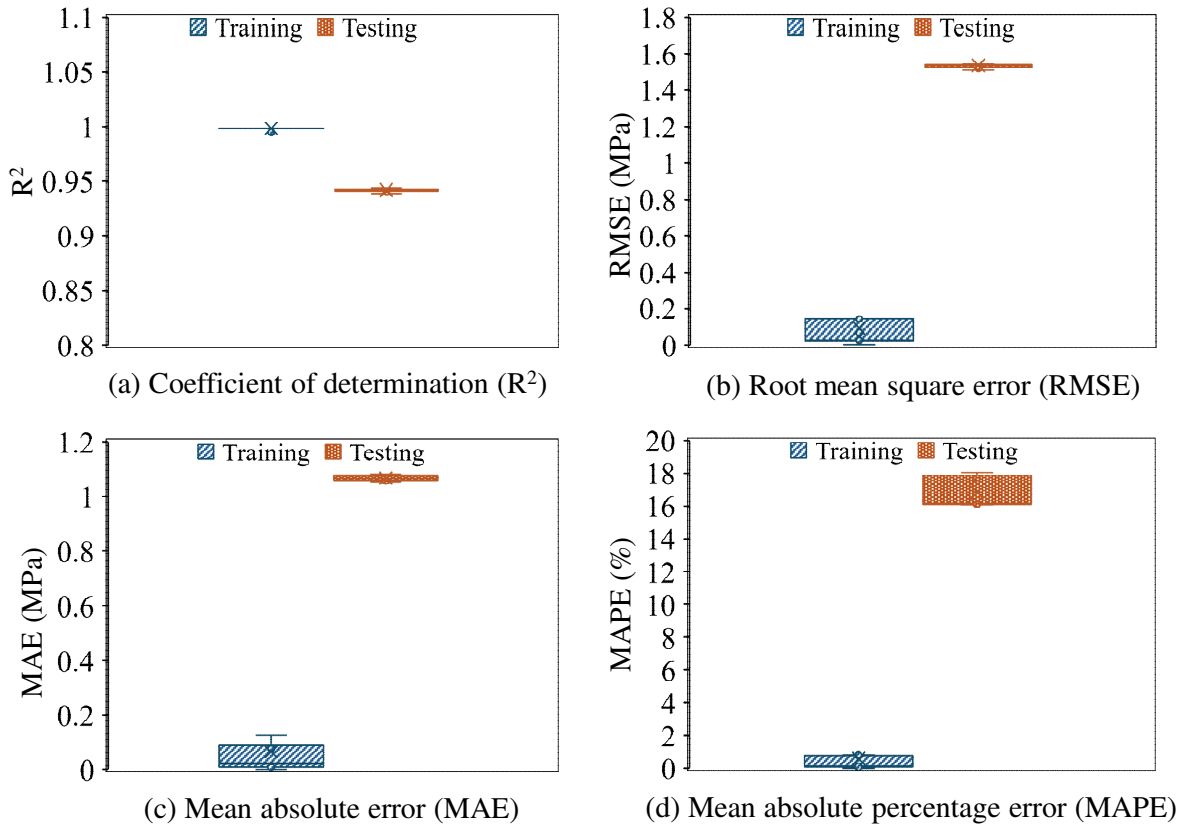


Fig. 9. Model framework used in this study.



(a) Coefficient of determination (R^2)

(b) Root mean square error (RMSE)

(c) Mean absolute error (MAE)

(d) Mean absolute percentage error (MAPE)

Fig. 10. Boxplots of the evaluation metrics obtained from ten independent runs of the proposed WOA–ETR model for the training and testing datasets.

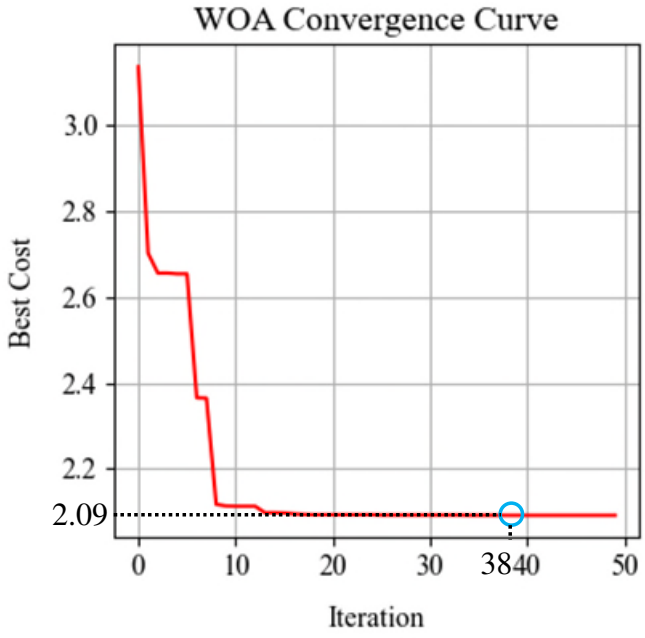


Fig. 11. Convergence curve of the WOA optimization process corresponding to the best-performing WOA–ETR model.

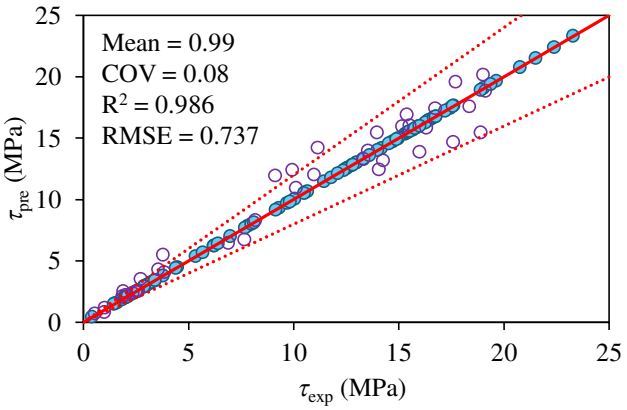
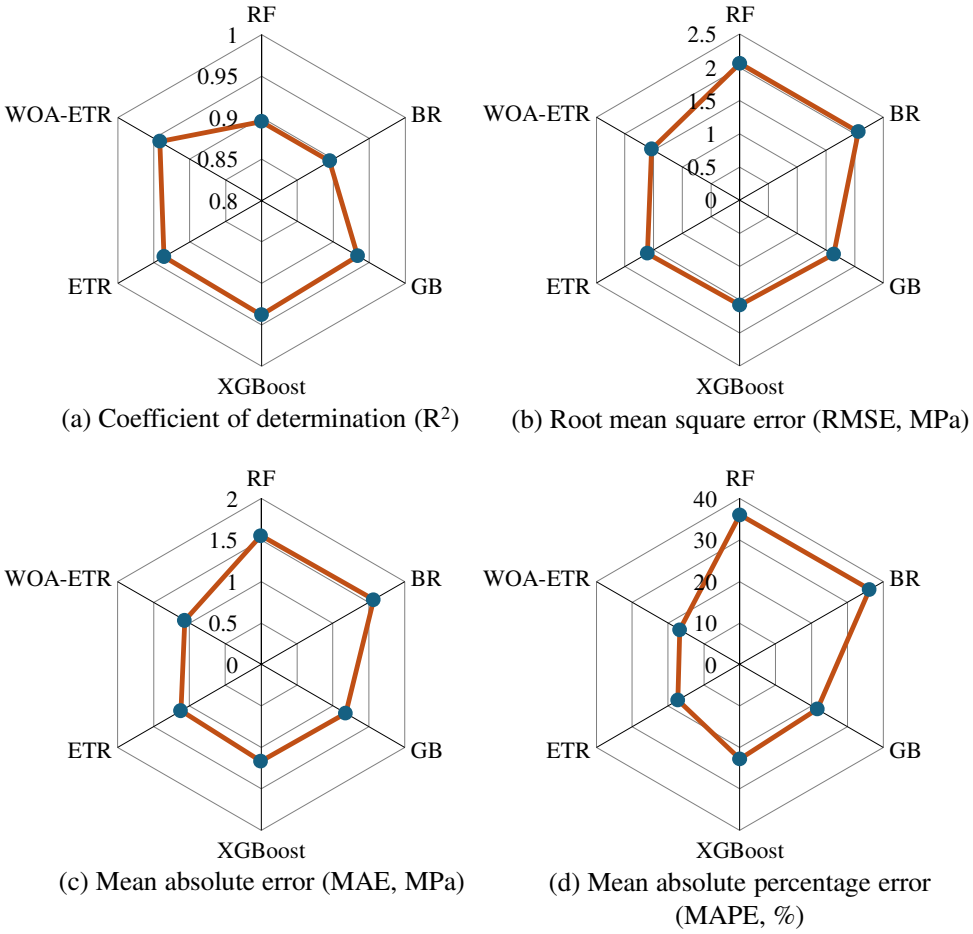


Fig. 12. Predictions by the best WOA-ETR model in comparison with experimental results.



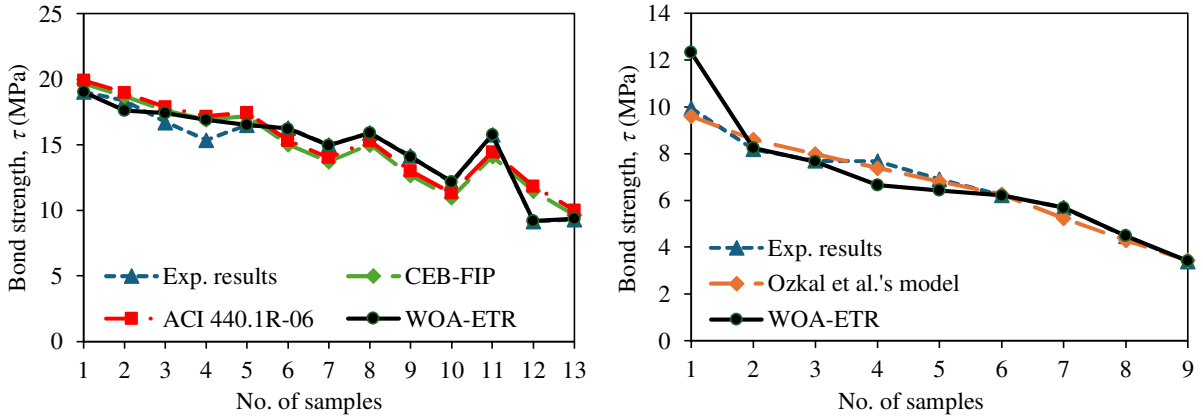
(a) Coefficient of determination (R^2)

(b) Root mean square error (RMSE, MPa)

(c) Mean absolute error (MAE, MPa)

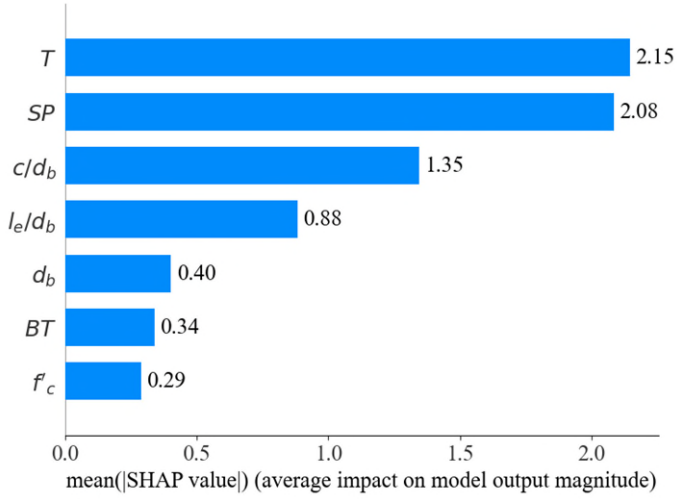
(d) Mean absolute percentage error (MAPE, %)

Fig. 13. Comparison of predictive performance of different ML models.

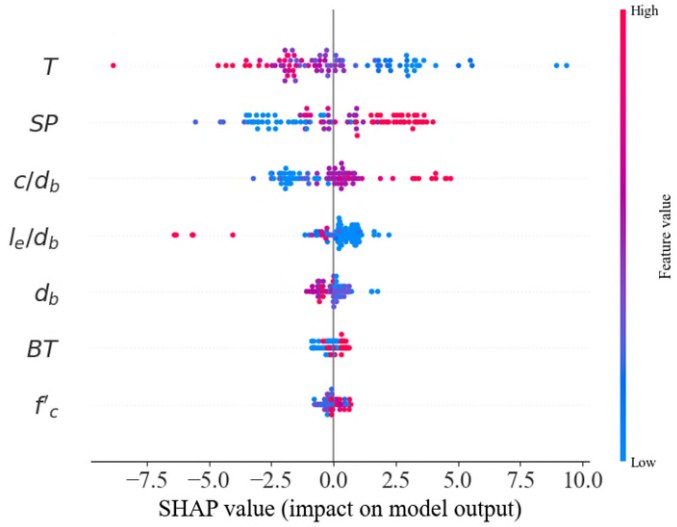


(a) Data from the study by El-Gamal (a) Data from the study by Ozkal et al.

Fig. 14. Comparison of bond strength predicted by WOA-ETR and mathematical models with experimental results.



(a) SHAP feature importance



(b) SHAP summary plot

Fig. 15. Global interpretation of bond strength predictions using the best-performing WOA–ETR model.

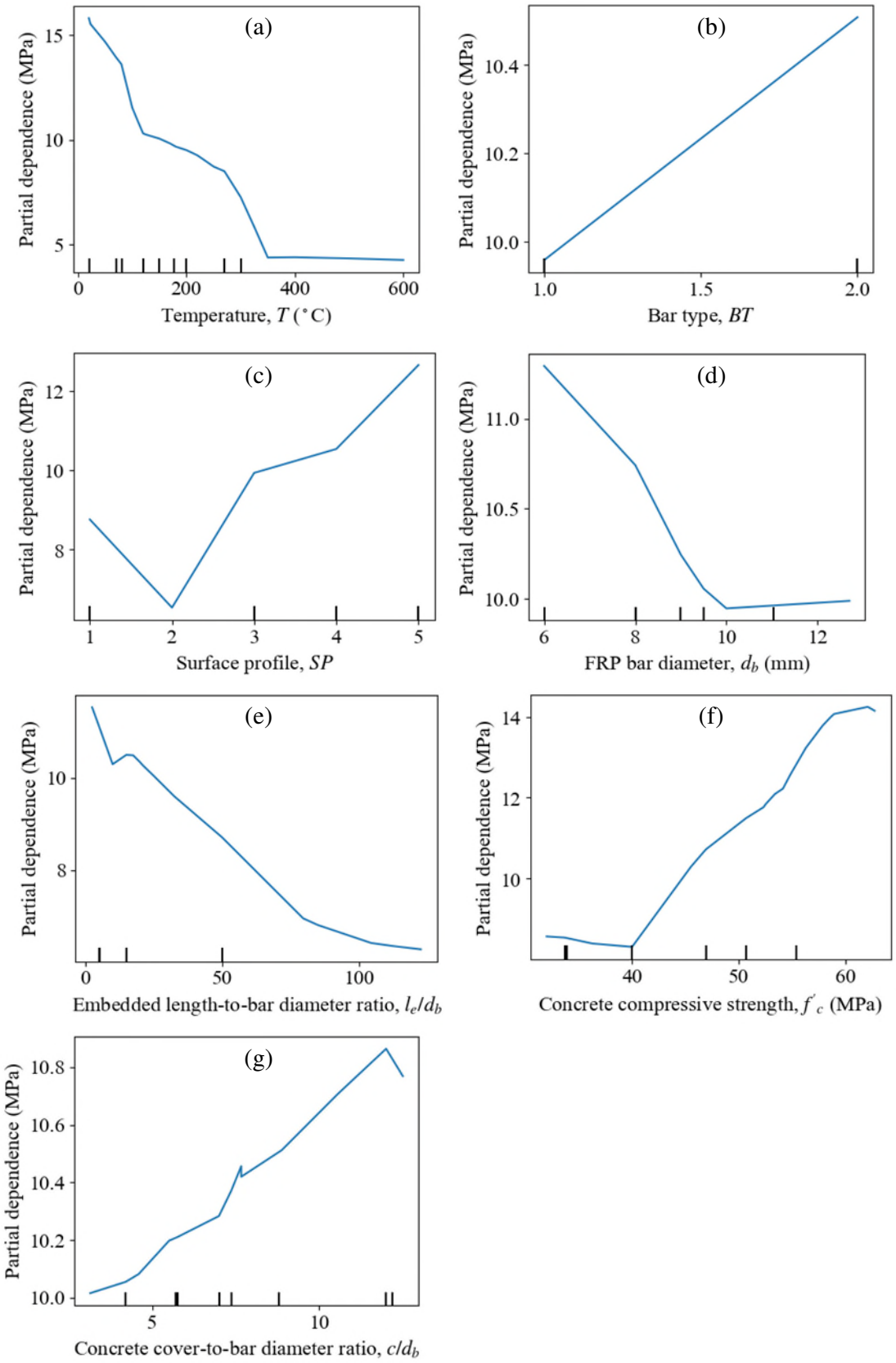


Fig. 16. Partial dependence plots of bond strength predictions using the best-performing WOA–ETR model.

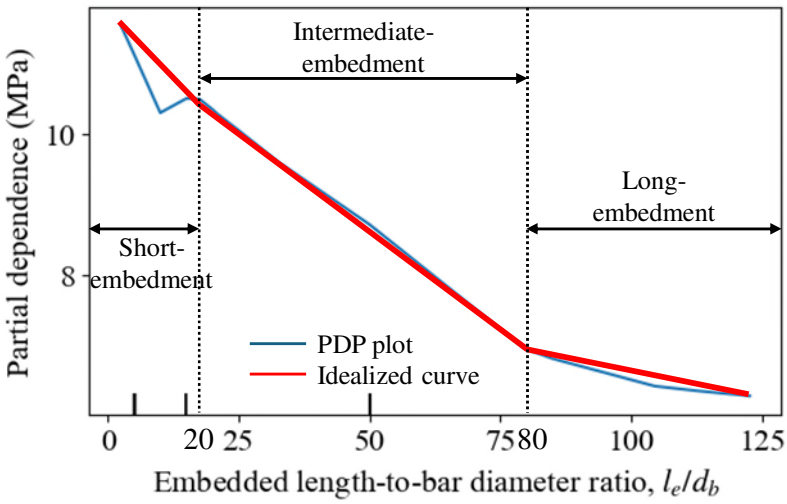


Fig. 17. Classification of the experimental database according to embedment length based on PDP analysis.

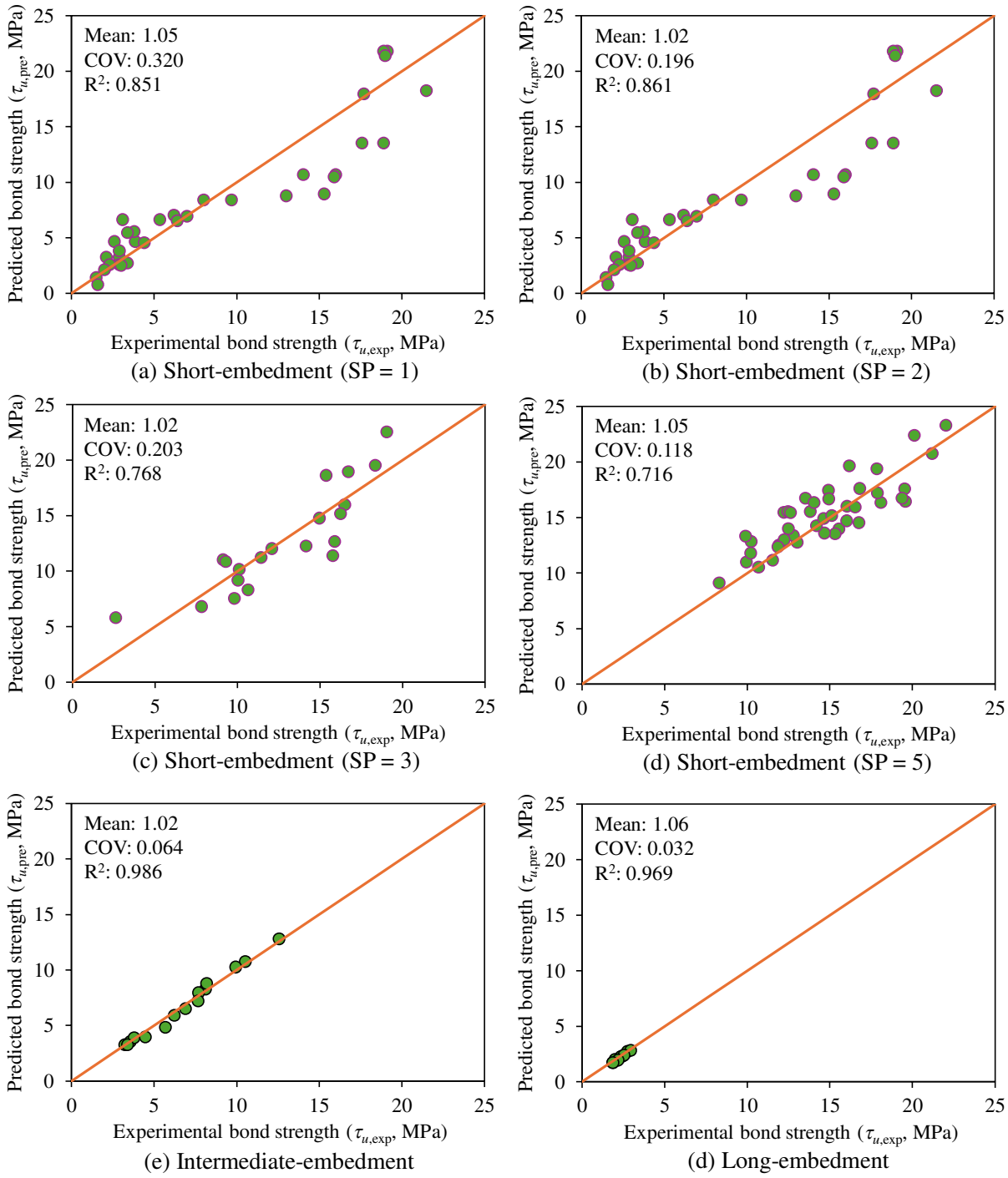


Fig. 18. Comparison of the proposed equation predictions with experimental results.